Materials Today Bio 25 (2024) 101005

Contents lists available at ScienceDirect

Materials Today Bio

journal homepage: www.journals.elsevier.com/materials-today-bio

Oxygen-producing and pH-responsive targeted DNA nanoflowers for enhanced chemo-sonodynamic therapy of lung cancer

Hongjian Liao [a,b,1], Yuchao Cao [a,b,1], Can Hu [a,b], Shangfeng Shen [a,b], Zhifei Zhang [a,b], Dairong Li [c,**], Yonghong Du [a,b,*]

[a] State Key Laboratory of Ultrasound in Medicine and Engineering, College of Biomedical Engineering, Chongqing Medical University, Chongqing, 400016, China
[b] Chongqing Key Laboratory of Biomedical Engineering, Chongqing Medical University, Chongqing, 400016, China
[c] Department of Respiratory and Critical Care Medicine, the First Affiliated Hospital of Chongqing Medical University, Chongqing, 400016, China

ARTICLE INFO

Keywords:
DNA nanoflower
Sonodynamic therapy
Lung cancer
Hypoxia
Active-targeting

ABSTRACT

Lung cancer is the deadliest kind of cancer in the world, and the hypoxic tumor microenvironment can significantly lower the sensitivity of chemotherapeutic drugs and limit the efficacy of different therapeutic approaches. In order to overcome these problems, we have designed a drug-loaded targeted DNA nanoflowers encoding AS1411 aptamer and encapsulating chemotherapeutic drug doxorubicin and oxygen-producing drug horseradish peroxidase (DOX/HRP-DFs). These nanoflowers can release drugs in response to acidic tumor microenvironment and alleviate tumor tissue hypoxia, enhancing the therapeutic effects of chemotherapy synergistic with sonodynamic therapy. Owing to the encoded drug-loading sequence, the doxorubicin loading rate of DNA nanoflowers reached 73.24 ± 3.45%, and the drug could be released quickly by disintegrating in an acidic environment. Furthermore, the AS1411 aptamer endowed DNA nanoflowers with exceptional tumor targeting properties, which increased the concentration of chemotherapeutic drug doxorubicin in tumor cells. It is noteworthy that both *in vitro* and *in vivo* experiments demonstrated DNA nanoflowers could considerably improve the hypoxia of tumor cells, which enabled the generation of sufficient reactive oxygen species in combination with ultrasound, significantly enhancing the therapeutic effect of sonodynamic therapy and evidently inhibiting tumor growth and metastasis. Overall, this DNA nanoflowers delivery system offers a promising approach for treating lung cancer.

1. Introduction

Currently, non-small cell lung cancer, which accounts for more than 80% of all lung cancer cases, is one of the most prevalent and fatal types of the disease worldwide [1,2]. Chemotherapy is still the primary treatment option for lung cancer therapy nowadays. Among chemotherapeutic drugs, doxorubicin (DOX), an anthracycline antibiotic, has been utilized in numerous studies for the treatment of lung cancer [3–5]. However, the clinical application of DOX still faces many difficulties that remain to be solved. In spite of this, DOX has detrimental side effects, including cardiomyopathy, which might cause congestive heart failure and death [6,7]. Specifically, the multidrug resistance of DOX poses a significant challenge to its application in cancer chemotherapy and decreased the efficiency of chemotherapy to eliminate tumor cells [8,9]. In recent years, combining DOX with other therapies based on secure and efficient delivery systems has become an effective strategy for cancer treatment [10,11].

DNA nanotechnology has found extensive use in a variety of fields, including bioimaging, drug delivery, and biomedicine, due to its facile synthesis, sequence programmability, high biostability and functional diversity [12–14]. DNA nanomaterials, which combine DNA strands with other nanomaterials and have uniform sizes and well-defined structures, have become novel nanomaterials for biomedicine. They have two- or three-dimensionally made DNA nanostructures, such as DNA nanoflowers, DNA origami, DNA tree-like molecules, DNA cages, and DNA nanoparticles [15–18]. The synthesis of DNA nanoflowers is based on the production of a high concentration of long DNA strands and the by-product magnesium pyrophosphate during an amplification

* Corresponding author. No. 1, Yixueyuan Road, Yuzhong District, Chongqing, 400016, China.
** Corresponding author. No. 1, Youyi Road, Yuzhong District, Chongqing, 400016, China.
E-mail addresses: lidairong@hospital.cqmu.edu.cn (D. Li), duyonghong@cqmu.edu.cn (Y. Du).
[1] These authors have contributed equally to this work.

https://doi.org/10.1016/j.mtbio.2024.101005
Received 30 November 2023; Received in revised form 7 February 2024; Accepted 19 February 2024
Available online 21 February 2024

reaction, and once the concentration of both products reaches a certain level, single-DNA molecule could condense to magnesium-pyrophosphate particles (as a core) that self-assemble into a flower-like structure through liquid crystallization. Furthermore, in an acidic environment, the magnesium pyrophosphate core of DNA nanoflowers disintegrates in a pH-responsive manner, thus allowing DNA nanoflowers to release the drug rapidly. Through elaborate template sequence design, DNA nanoflowers can be engineered to perform a range of applications, including fluorescence imaging, drug delivery, and specific recognition [19–21]. DNA nanoflowers have been used effectively in the field of tumor therapy because of their high loading capacity and remarkable biological stability [13,22].

Hypoxia, one of the common features of the tumor microenvironment in the majority of solid tumors, is brought on by the tumor cells' excessive oxygen consumption in the acidic environment and the development of malformed blood vessels within the tumor tissue, which further reduces the oxygen supply to the tumor tissue [23,24]. Research have demonstrated that hypoxia plays a crucial role in the growth and metastasis of tumor [25]. In addition, the hypoxic microenvironment dramatically lessens the therapeutic effect on tumor cells, including chemotherapy and photodynamic therapy [26].

Sonodynamic therapy (SDT) is a novel therapeutic approach, which can exert toxic effect on tumor cells and bacteria by utilizing low-intensity ultrasound to irradiate an acoustic sensitizer to produce reactive oxygen species (ROS). Current studies have shown that the chemotherapeutic drug DOX can be used as an ultrasound sensitizer to enhance sonodynamic induced DNA damage, cell apoptosis, and the production of ROS and hydroxyl radicals [27]. It is of great significance to note that oxygen (O_2) is one of the primary sources of ROS in the mechanism of SDT [28]. Compared with photodynamic therapy, ultrasound energy can penetrate deeper tissues to achieve better therapeutic effect [29]. Besides, SDT offers the advantages of non-invasive and low side effects [30,31]. However, since SDT itself is an oxygen-consuming process and the tumor site is extremely hypoxic, it will be severely hampered to produce sufficient ROS during SDT, thus seriously weakening the therapeutic effect of SDT.

Hypoxia-mediated tumor resistance to various therapeutic modalities has been solved by manipulating the hypoxic microenvironment of the tumor through a range of oxygen delivery or production strategies. Specifically, hyperbaric oxygen therapy, oxygen-carrying nanosystems (oxygen-carrying nanobubbles, hemoglobin and perfluorocarbons, *etc*.) and enzymes (catalase, horseradish peroxidase (HRP)) that produce oxygen in situ at the tumor site are included, *etc* [32–36]. All of these strategies are effective in alleviating tumor tissue hypoxia and enhancing the efficacy of various tumor treatment modalities. These approaches, however, still have certain drawbacks, such as the side effects (oxygen toxicity) of hyperbaric oxygen therapy, the release of toxic substances from cell-free hemoglobin when loaded with oxygen for an extended period of time, and the poor biosafety of manganese dioxide [37]. Consequently, it is essential to develop a reliable and effective oxygen delivery route.

In this study, we prepared a DNA nanoflowers drug delivery system embedded AS1411 aptamer sequence in DNA template, which can actively target tumor cells and enhance the efficacy of chemotherapy synergistic with sonodynamic therapy by alleviating tumor hypoxia. DNA nanoflowers were designed to bind to DOX at the drug delivery site in the template sequence of DNA nanoflowers, while the AS1411 sequence of DNA nanoflowers can binds to nucleolin on the surface of cancer cells, thus allowing DNA nanoflowers have high drug loading rate and precisely deliver drug to tumor sites [38,39]. Moreover, the acidic microenvironment of the tumor can disintegrate the magnesium pyrophosphate skeleton of the DNA nanoflowers, making it possible to achieve effective controlled release of the drug. After being loaded by DNA nanoflowers, the catalytic activity and stability of HRP was remarkably increased, which could catalyze the oxygen generation from endogenous H_2O_2 in tumors, effectively alleviate tumor hypoxia and down-regulate the expression of HIF-1α, VEGF and CD31. More importantly, DOX, as an acoustic sensitizer under the action of ultrasound, can generate ROS, trigger apoptosis and ameliorate the vascular abnormalities of tumor tissues [40]. Sonodynamic therapy can not only trigger the generation of ROS, but also increase tumor permeability under the effect of cavitation in order to promote more chemotherapy drugs to enter tumor cells and improve chemotherapy effect [41]. This research demonstrated that our multifunctional DNA nanoflowers are biosafe and stable enough to significantly enhance the inhibition of tumor growth caused by synergistic chemotherapy and sonodynamic therapy *in vivo and in vitro*. Scheme 1 depicts the therapeutic principle for the ultrasound therapy approach combined with multifunctional DNA nanoflowers.

2. Experimental section

2.1. Materials

The DNA oligonucleotide sequence is listed in Table S1 and was synthesized and purified by Shanghai Sangon Biotech Co., Ltd. T4 DNA ligase was purchased from Takara Biomedical Technology (Beijing) Co., Ltd. (China). phi29 DNA polymerase was purchased from New England Biolabs Beijing Co., Ltd. (China). dNTPs and Bradford protein detection kit were purchased from Shanghai Sangon Biotech Co., Ltd. (China). HRP, tris (4,7-biphenyl-1,10-phenanthroline) ruthenium dichloride ($[(Ru(DPP)_3)]Cl_2$) and Matrigel Basement Membrane Matrix were purchased from Shanghai Aladdin Biochemical Technology Co., Ltd. (China). Fetal bovine serum (FBS), DMEM medium and streptomycin/penicillin were purchased from Beijing Solarbio Science & Technology Co., Ltd. (China). Cell counting kit-8 (CCK-8) was purchased from Dojindo. (Japan). Transwell plates were purchased from Corning Incorporated (USA).

2.2. Cell culture and animal model establishment

The murine Lewis lung carcinoma (LLC) cell line was purchased from Shanghai Fuheng Biotechnology Co., Ltd, and the human normal bronchial epithelioid cell line (16HBE) was provided by Oncology and Epigenetics Laboratory of Chongqing Medical University. Both cells were cultured in DMEM containing 10% FBS and 1% streptomycin/penicillin at 37 °C in a normoxic (21% O_2) humid atmosphere with 5% CO_2. In addition, the hypoxic (1% O_2) humid atmosphere created by an AnaeroGen bag.

Male C57BL/6 mice (6–8 weeks old, 16–21 g in weight) were purchased from and raised at the Animal Experiment Center of Chongqing Medical University. The murine Lewis lung adenocarcinoma model was established by subcutaneous injection of LLC cells (1×10^7 cells in 100 μL) into the right side of C57BL/6 mice. This study complied with the ethical standards established by the Experimental Animal Ethics Committee of Chongqing Medical University (Ethical Number: 2,022,152).

2.3. Preparation of the circular DNA template

Phosphorylated DNA template (1 μM) and primer (1.5 μM) were hybridized in 1 × T4 DNA ligase reaction buffer (66 mM Tris-HCl, 6.6 mM $MgCl_2$, 10 mM Dithiothreitol and 0.1 mM adenosine triphosphate) by heating at 95 °C for 5 min, and then gradually cooled to room temperature. Subsequently, T4 DNA ligase was then added, and the mixture was allowed to incubate at 16 °C overnight, then T4 DNA ligase was inactivated by reaction at 65 °C for 10 min.

2.4. Preparation of HRP-DFs and DOX/HRP-DFs

The HRP-encapsulated DNA nanoflowers (termed HRP-DFs) were synthesized by the RCA reaction. The circular DNA template (0.5 μM), Phi29 DNA polymerase (1 U/μL), dNTP mixture (1 mM) and HRP solution (0.5 mg/mL) were incubated in Phi29 DNA polymerase reaction

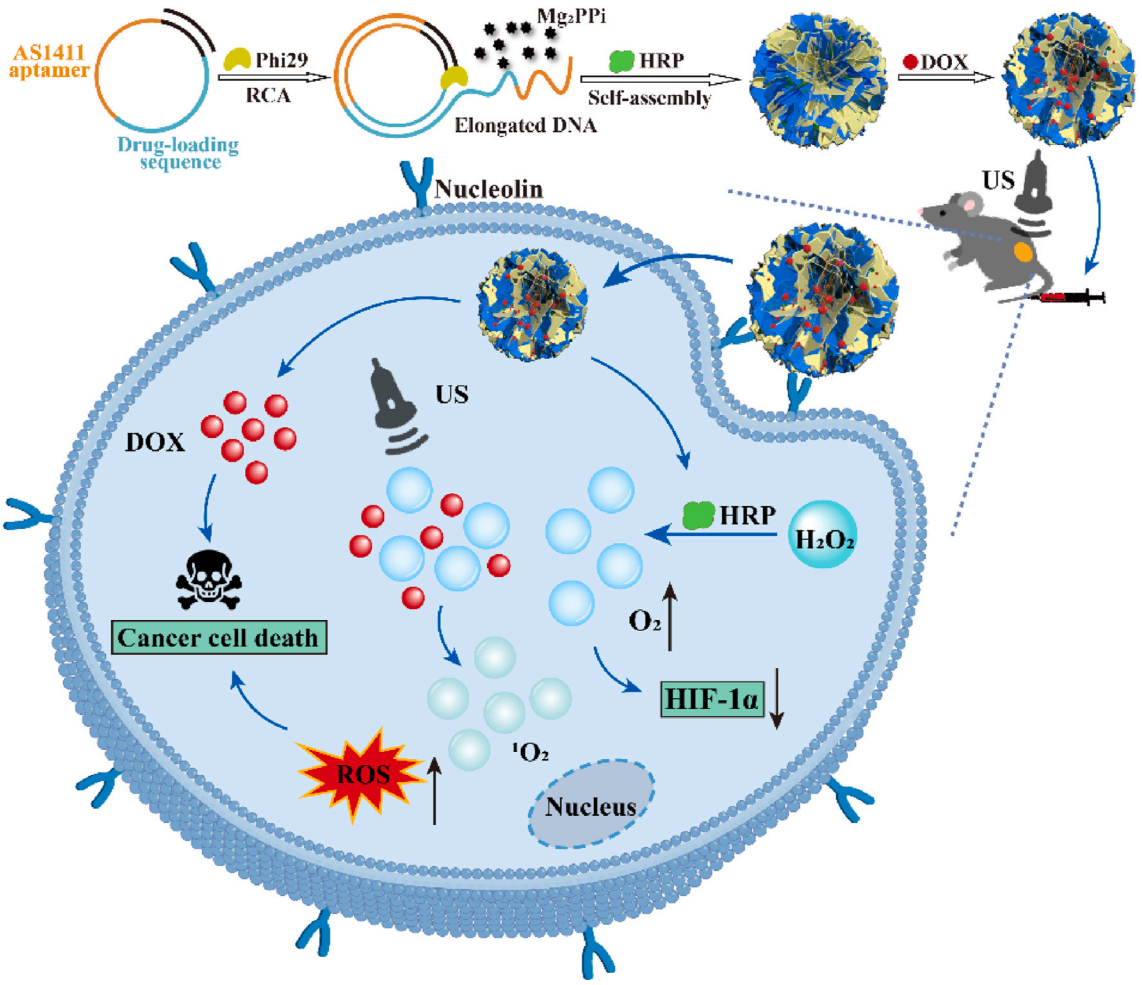

Scheme 1. The schematic illustrations of multifunctional DNA nanoflowers combined with US therapy strategy.

buffer (66 mM Tris-HCl, 6.6 mM $MgCl_2$, 10 mM Dithiothreitol and 0.1 mM adenosine triphosphate) at 30 °C for 10 h. Then the reaction was terminated by heating at 65 °C for 10 min to inactivate Phi29 DNA polymerase. The HRP-DFs were washed three times with deionized water by centrifugation at 10000 rpm for 10 min and then stored at 4 °C. And the blank DNA nanoflowers were prepared by replacing HRP with bovine serum albumin (BSA). Doxorubicin (DOX) was mixed with HRP-DFs and incubated at room temperature for various durations to precipitate DOX/HRP-DFs. These DNA nanoflowers are classified as either DOX/HRP-DFs (targeted) or DOX/HRP-NADFs (untargeted) depending on whether the AS1411 aptamer sequence is encoded in the DNA template or not. And FITC-conjugated UTP and Cy5.5-conjugated UTP were added to the RCA reaction system to create FITC-DOX/HRP-DFs and Cy5.5-DOX/HRP-DFs.

2.5. Characterization of DOX/HRP-DFs

The successful synthesis of DOX/HRP-DFs was confirmed by 2% agarose gel electrophoresis. And the external morphology and internal structure of DOX/HRP-DFs were observed by scanning electron microscopy (SEM, Hitachi, Japan) and transmission electron microscopy (TEM, Hitachi, Japan). Then the average size and zeta potential of DOX/HRP-DFs were detected by dynamic light scattering (DLS, Malvern instruments, UK). Additionally, the elemental compositions of DOX/HRP-DFs were analyzed by energy dispersive X-ray spectroscopy (EDS, Hitachi, Japan). HRP content in DOX/HRP-DFs was detected by Bradford protein detection kit.

2.6. Investigation of drug loading and release from DNA nanoflowers

In the process of preparing DOX/HRP-DFs, DOX (1 mg/mL) was mixed with HRP-DFs and incubated at room temperature for various durations, and then centrifuged at 15000 rpm for 15 min. The free DOX in the supernatant was quantified by measuring the absorbance at 480 nm using UV–vis spectrophotometry (UV-2600 SHIMADZU, Japan). The amount of DOX loaded in DOX/HRP-DFs was calculated by subtracting the amount of DOX in the supernatant from total amount of DOX.

The amount of HRP in DOX/HRP-DFs was measured by Bradford Protein Assay Kit, in brief, the samples were mixed with Bradford's working solution for 5 min to measure the absorbance at 595 nm, and the standard curve was determined by the standard protein provided. Encapsulation efficiency (%) was obtained from the ratio of the amount of HRP added to the total amount of HRP used.

Given the favorable pH-responsive properties of DNA nanoflowers, the effect of different pH on the DOX release from DOX/HRP-DFs was investigated by a dialysis method. DOX/HRP-DFs was resuspended with deionized water and transferred to different dialysis bags (8–14 kDa MWCO). Then the dialysis bags were placed in 20 mL PBS (pH either 7.4, 6.8 or 5.5) in a breaker and shaken at 100 rpm at 37 °C. At various time points (0.25, 0.5, 1, 2, 4, 8, 12, 24, 48 h), 300 μL dialysate was sampled to detect the concentration of released DOX in each sample and the release efficiency were counted as follows: Drug release (%) = (DOX amount in dialysate/initial DOX amount in DOX/HRP-DFs) × 100%.

2.7. In vitro cytotoxicity assay

The cell viability *in vitro* was tested using the cell counting Kit-8 (CCK-8) assay to analyze of cytotoxicity of different samples. LLC cells were inoculated in 96-well culture plates for 24 h. For chemotherapy, the cells were treated with serum-free medium containing free DOX, DOX-DFs and DOX/HRP-DFs (DOX with final concentration of 0.5, 1, 2, 4, 8 μg/mL) for 4 h under normoxia (21% O_2) or hypoxia (1% O_2), respectively. Then the cells were cultured for an additional 24 h, washed with PBS, and then 100 μL of the medium containing 10% CCK-8 reagent was added to each sample well in the 96-well plate for incubation for another 2 h. The absorbance value of all samples in the plate at 450 nm wavelength was detected by the Multifunctional Enzyme Labeling Instrument to determine the cell survival rate. For the sonodynamic therapy experiment, LLC cells were treated with above different drugs under normoxia (21% O_2) or hypoxia (1% O_2) for 4 h, and then were irradiated with ultrasound (1 MHz, 1W/cm^2) (Ultrasound extracorporeal noninvasive therapeutic instrument developed by Chongqing Ronghai Engineering Research Center of Ultrasound Medicine, and the instrument model is USR-2) for 3 min. Following treatment, the cell culture was carried out for a further 24 h, and then cell survival was measured with CCK-8 reagent. The cell activity was calculated by the following formula: Cell viability (%) = $(OD_{treated} - OD_{blank})/(OD_{control} - OD_{blank}) \times 100\%$

In addition, the toxic effects of different samples *in vitro* on LLC cells under hypoxia were observed by confocal laser scanning microscopy (CLSM, Nikon A1, Japan). LLC cells were inoculated in CLSM dishes for 24 h. Then LLC cells were subjected to the same treatment as described above under hypoxia conditions (1%O_2), and the cells were stained with Calcein-AM/PI live-dead cell double-staining kit at the end of the treatment, and the survival and death of cells in different treatment groups was observed by CLSM.

2.8. In vitro apoptosis

Apoptosis induced by different samples in hypoxic environment was detected by flow cytometry. LLC cells at logarithmic growth stage were inoculated in six-well culture plates at 1×10^6 cells/well density. For chemotherapy, cells were treated with PBS, free DOX, DOX-DFs and DOX/HRP-DFs (DOX with final concentration of 0.5, 1, 2, 4, 8 μg/mL) for 4 h under hypoxia (1% O_2), respectively. Then cells were digested with trypsin and stained with Annexin V-fluorescein and 4′,6-diamidino-2-phenylindole (DAPI). For the sonodynamic therapy experiment, LLC cells were treated with above different drugs under hypoxia (1% O_2) for 4 h, and then were irradiated with 1 MHz ultrasound with intensity of 1 W/cm^2 for 3 min. The cell staining procedure was the same with the one in chemotherapy. Finally, all samples were assayed by flow cytometry (Beckman Coulter, Inc., USA).

2.9. Therapeutic effect evaluation of DOX/HRP-DFs combined ultrasound irradiation

When the tumor volumes reached 100–150 mm^3, all C57BL/6 tumor-bearing mice were randomly divided into eight groups: PBS (control); ultrasound alone (US); free DOX; free DOX + US; DOX-DFs; DOX-DFs + US; DOX/HRP-DFs; and DOX/HRP-DFs + US. Mice with different treatments were administered by injecting various medications into the mice's tail veins, and the tumor site of mice in the group associated ultrasound were irradiated ultrasound (1 MHz, 1 W/cm^2) for 3 min at 24 h after drug injection during experiments. The weight and tumor volume of mice were monitored every 2 days, and tumor volume was figured out as follows: tumor volume (mm^3) = (Length × Width^2)/2. The mice tumors in each treatment group were harvested and photographed following the course of treatment. After paraffin embedding, sections from tumor tissue were cut in order to conduct hematoxylin-eosin (H&E) staining, immunohistochemical staining and immunofluorescence experiments. To examine the apoptosis, TdT-mediated dUTP nick end labeling (TUNEL) was used to stain tumor cells by immunofluorescence staining. Additionally, tumor tissue slices were immunohistochemical stained for hypoxia-inducible factor-1α (HIF-1α), vascular endothelial growth factor (VEGF) and platelet-endothelial cell adhesion molecule-1 (PECAM-1/CD31) using the appropriate antibodies, as directed. In the meantime, the eyeballs of the mice in each group were removed, and blood was taken. And the level of HIF-1α, VEGF and CD31 in serum was detected by mouse HIF-1α, VEGF and CD31 ELISA kit. Additionally, the survival rate of tumor-bearing mice in each treatment group was checked daily during the observation period of 60 days.

2.10. In vivo biosafety test

At the end of the treatment, the vital organs (heart, liver, spleen, lung, and kidney) of mice in each group were collected and made into paraffin sections for H&E staining to evaluate the biosafety of the nanoflowers. Meanwhile, the levels of biochemical indicators such as alanine aminotransferase (ALT), aspartate aminotransferase (AST), blood urea nitrogen (BUN), creatinine (CREA), creatine kinase (CK), and total bilirubin (TBIL) were all measured in mice' serum.

2.11. Statistical analysis

All data were expressed as mean ± standard deviation (SD) and statistical analysis was performed using GraphPad Prism version 8.00 for Windows (GraphPad Software; La Jolla, CA, USA). Significant differences among groups were analyzed using a one-way ANOVA and differences for individual groups were determined using Student's t-test. The results were regarded as a significant difference when $^*P < 0.05$. $^{**}P < 0.01$, $^{***}P < 0.001$.

3. Experimental results

3.1. Characterization of DOX/HRP-DFs

The circle-DNA and high molecular weight products synthesized by the RCA reaction were characterized by 2% agarose electrophoresis. As shown in Fig. 1a, the long-stranded DNA in lane 2 was stagnant in the hole due to its larger molecular weight after the RCA reaction and thus, the DNA loop product in lane 3 moved slower than the DNA template strand in lane 4, demonstrating the generation of loop DNA. The DLS results showed that the HRP-DFs, with a particle size at 396 ± 8 nm and a potential at −17.4 ± 1.2 mV, and the DOX/HRP-DFs, with a particle size at 415 ± 9 nm and a potential at −13.3 ± 2.2 mV, demonstrated that loading DOX had little effect on the particle size of DNA nanoflowers (Fig. 1b and c and Fig. S1). The structure and morphology of DOX/HRP-DFs were analyzed by SEM and TEM (Fig. 1d and e), and the results showed that the prepared DOX/HRP-DFs had a flaky porous flower-like structure. These porous structures allow for the loading of drug (e.g. DOX). Furthermore, the structures of blank DFs, HRP-DFs and DOX-DFs were also analyzed by TEM, and the results show that the encapsulation of HRP and DOX does not affect the morphology and structure of DNA nanoflowers (Fig. S2). In addition, the constituent elements of DOX/HRP-DFs were analyzed by EDS (Fig. 1f), and the elements C, N, O, P, and Mg are main elements of the DNA backbone and magnesium pyrophosphate in DOX/HRP-DFs. What's more, the EDS elemental mapping showed that the above elements were homogeneously distributed in the DOX/HRP-DFs (Fig. S3). To determine the amount of DNA in DOX/HRP-DFs, the absorbance of residual dNTP at 260 nm was measured to calculate the consumption of dNTP, and 87.02% of dNTP was consumed after 10 h reaction. The amount of HRP encapsulation detected by Bradford Protein Assay Kit was 50.8 ± 1.6 μg/mL, and the encapsulation efficiency was 10.2%.

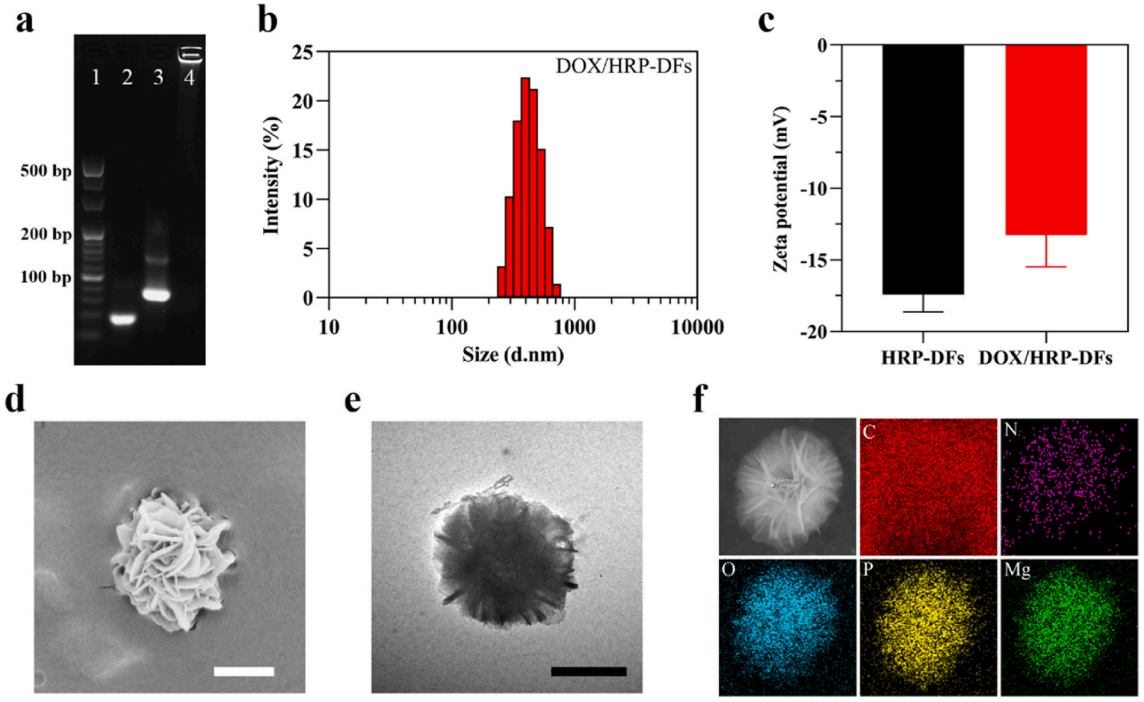

Fig. 1. Characteristics of DNA nanoflowers. (a) Products visualized by 2% agarose gel-electrophoresis (lane1: DNA marker, lane2: DNA template, lane3: Ligated DNA circle, lane4: DOX/HRP-DFs). (b) The average diameter distribution of DOX/HRP-DFs. (c) *Zeta* potential of HRP-DFs and DOX/HRP-DFs. (d) SEM images of DOX/HRP-DFs (scale bar = 500 nm). (e) TEM images of DOX/HRP-DFs. (scale bar = 500 nm). (f) EDS elemental mapping of DOX/HRP-DFs.

3.2. Stability detection of DOX/HRP-DFs

The stability of DNA nanoflowers is critical in the complex transport environment *in vivo*. After being incubated for 12 and 24 h with 10% FBS and DNase I (5 U/mL), DOX/HRP-DFs were characterized by 2% agarose electrophoresis (Fig. 2a). The results showed that DOX/HRP-DFs did not decompose after treatment with FBS and DNase I, implying that DOX/HRP-DFs had high serum stability and anti-enzymatic ability.

3.3. Drug loading and pH responsive release of DOX/HRP-DFs

The loading of DOX into DOX/HRP-DFs was quantified by a UV–vis spectrophotometer. As shown in Fig. 2b, the free DOX was loaded into HRP-DFs rapidly within around 30 min, and the drug loading efficiency in DOX/HRP-DFs was 73.24 ± 3.45%. After that, the loading efficiency of DOX remained essentially unchanged. The high loading rate is due to the porous structure of the DNA nanoflowers and the designed DNA template containing the drug-loading sequence. The DNA template designed in this study contains consecutive CG base pairs providing binding sites for DOX, and it is calculated that 42.10 ± 1.97% of DOX is loaded by binding to the drug binding sites, while the remaining DOX is loaded into the porous structure of DOX/HRP-DFs by physical encapsulation.

Next, the pH-responsive drug release ability of DOX/HRP-DFs was investigated. The stability of DOX/HRP-DFs in different pH was investigated with 2% agarose electrophoresis, which showed that DOX/HRP-DFs remained stable at pH 7.4, while decomposition occurred at pH 5.5 (Fig. 2d). In addition, the drug release experimental results showed that at physiological pH (pH = 7.4), DOX/HRP-DFs were more stable and the release rate of DOX was only 21.71 ± 1.03% (Fig. 2c), and at pH 6.8, the DOX release rate of DOX/HRP-DFs was 29.18 ± 1.12%. However, under acidic conditions (pH = 5.5), the release rate of DOX increased rapidly, with a cumulative release of 82.42 ± 1.07%. It was demonstrated that DOX/HRP-DFs have good pH response characteristics and high stability under physiological conditions, which can prevent the early release and diffusion of DOX in surrounding normal cells.

3.4. Detection of catalytic activity of HRP in HRP-DFs

The catalytic activity of HRP-DFs was evaluated by measuring the catalytic rate of H_2O_2 oxidation of ABTS. As shown in Fig. 2e, when the reaction time was 20 min, the absorption peak of HRP-DFs in the spectral range of 350 nm–500 nm was significantly higher than that of free HRP and the mixture of HRP and blank DFs, indicating that the catalytic efficiency of HRP-DFs was better than that of free HRP and the mixture of HRP and blank DFs.

3.5. Oxygen production capacity evaluation

HRP, as a biocatalyst, can catalyze the conversion of H_2O_2 into H_2O and O_2. In this experiment, the ability of DOX/HRP-DFs to catalyze the conversion of H_2O_2 to O_2 was investigated by a portable dissolved oxygen meter. The oxygen production of blank DFs and free DOX was similar to that of the control group, indicating that blank DFs and free DOX could not catalyze H_2O_2 to O_2 production (Fig. 2f). In contrast, a significant amount of O_2 was produced when free HRP and DOX/HRP-DFs mixed with H_2O_2, and DOX/HRP-DFs could generate more O_2 than free HRP. At the same time, the generation process of O_2 during the reaction was tracked in the centrifuge tube, and visual inspection revealed that the number of bubbles in the tube of DOX/HRP-DFs was also significantly higher than that of free HRP (Fig. 2g).

Intracellular O_2 production of DOX/HRP-DFs was detected by $[(Ru(dpp)_3)]Cl_2$ probe, whose fluorescence would be sensitively dampened by oxygen molecules. As depicted in Fig. 3a and b. The red fluorescence of LLC cells in hypoxic environment was more obvious. After the addition of free HRP and DOX/HRP-DFs, the intensity of the red fluorescence in LLC cells dramatically decreased, and the fluorescence intensity of the DOX/HRP-DFs group was weaker than that of the free HRP group. And the semi-quantitative results of fluorescence intensity also supported the previous experimental findings by showing that DOX/HRP-DFs had higher catalytic efficiency than free HRP.

In addition, hypoxia-inducible fact-1α (HIF-1α) is a major factor reflecting the degree of tumor hypoxia, and Western blotting analysis

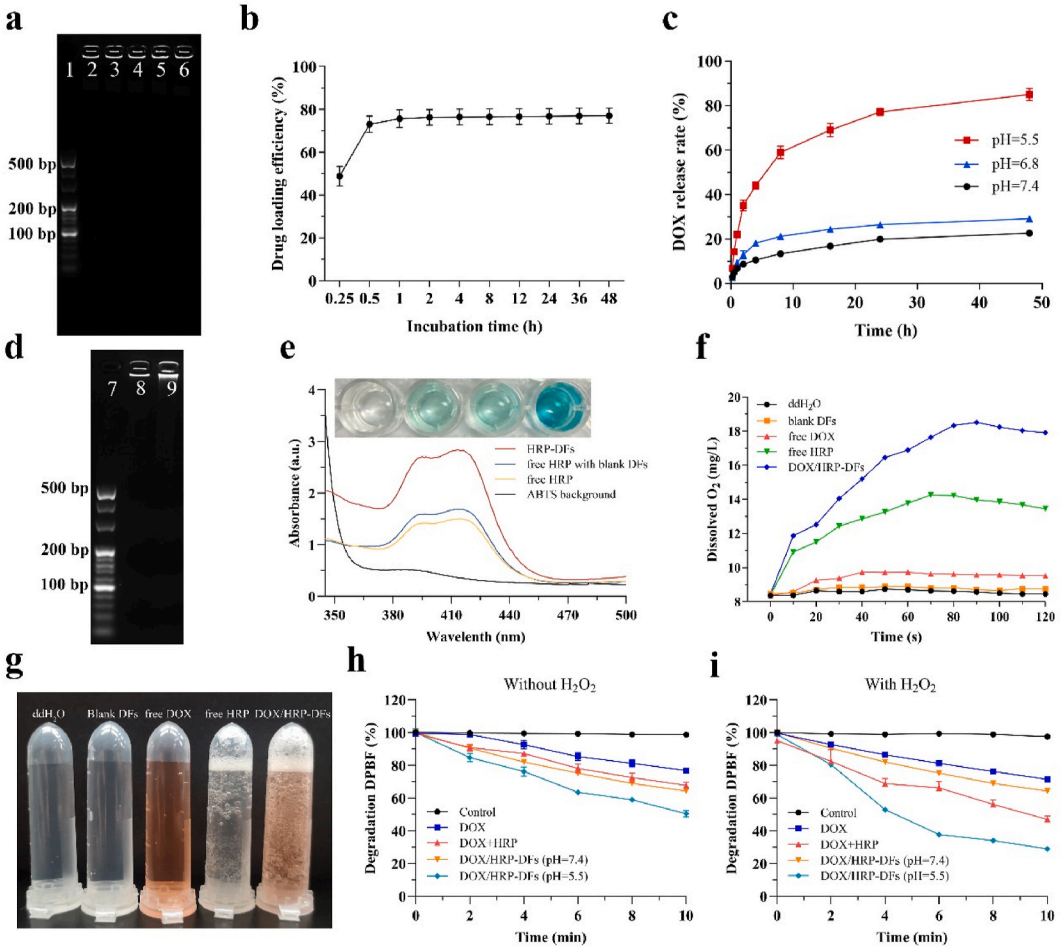

Fig. 2. (a). the stability of DOX/HRP-DFs was analyzed by 2% agarose electrophoresis. (lane 1: DNA marker, lane 2 and lane 3: DOX/HRP-DFs in 10% FBS for 12 h and 24 h, lane 4 and lane 5: DOX/HRP-DFs in 5 U/mL DNase I for 12 h and 24 h, lane 6: DOX/HRP-DFs in PBS for 24h). (b). DOX/HRP-DFs loading DOX efficiency in different time points. (c). DOX release in different pH (5.5, 6.8 or 7.4). (d). 2% agarose electrophoresis analysis of DOX/HRP-DFs at different pH (lane 7: DNA marker, lane 8: pH = 7.4, lane 9: pH = 5.5). (e). Corresponding UV–vis absorption spectra at the reaction time of 20 min. (f). Detection the oxygen production of DOX/HRP-DFs by a portable dissolved oxygen meter. (g). Photograph of oxygen generation. (h) and (i). Extracellular ROS generation by detecting DPBF consuming without H_2O_2 (h) and with H_2O_2 (i).

verified that DOX/HRP-DFs were able to significantly down-regulate the expression of HIF-1α in hypoxic LLC cells (Fig. 5g), which reconfirmed that DOX/HRP-DFs have ability to alleviate the hypoxia of tumor cells and enhance the efficacy of SDT.

3.6. Extracellular and intracellular ROS production

DPBF reagent was used to assess extracellular ROS production of DOX/HRP-DFs. As depicted in Fig. 2h, when H_2O_2 was absent, the DPBF content in the control group showed no significant decrease after irradiation, while the concentration of DPBF in the free DOX, mixed free DOX and HRP, and DOX/HRP-DFs (pH 7.4) decreased significantly with the increase of time after ultrasonic irradiation, which proved that the *in vitro* generation of singlet oxygen ($^1O_2$) under action of ultrasound on the sound sensitizer (DOX). In addition, when H_2O_2 was added, more DPBF was consumed in the mixed free DOX and HRP, and DOX/HRP-DFs (pH 7.4) groups, which proved that the system could boost O_2 level via HRP-enabled H_2O_2 decomposition and consequently increase further $^1O_2$ production (Fig. 2i). It was also found that $^1O_2$ was produced at pH 7.4, which may be related to the release of HRP in DOX/HRP-DFs brought on ultrasonic irradiation. The amount of $^1O_2$ produced in DOX/HRP-DFs at pH 5.5 was substantially higher than at pH 7.4, indicating that the pH-responsive drug release properties of DOX/HRP-DFs are more important for SDT. This experiment shows that DOX/HRP-DFs can produce ROS after being exposed to ultrasound, and that the ability of DNA nanoflowers to synthesize oxygen and to release controlled amounts of drugs can improve the therapeutic effects of SDT.

Next, ROS production in LLC cells was detected using the DCFH-DA probe. The results from CLSM observation showed that free DOX was able to produce ROS, and that when the intracellular drug concentration grew, more ROS could be produced after the addition of DOX/HRP-DFs (Fig. 3c and d). In addition, the green fluorescence produced by each experimental group increased significantly after ultrasound irradiation, with the DOX/HRP-DFs showing the highest level of green fluorescence compared with other groups, demonstrating that DOX/HRP-DFs combined US could generate the most ROS in cells. According to flow cytometry, cells treated with DOX/HRP-DFs in combination with US had the highest fluorescence intensity when compared to other treatments. It demonstrates how DOX/HRP-DFs can generate ROS and enhance therapeutic effects of SDT.

3.7. Specific cellular uptake of DOX/HRP-DFs

The key to precision therapy lies in targeted drug delivery, which boosts SDT treatment effectiveness and lessens cytotoxicity effects on neighboring healthy tissues. The nucleolin on the surface of tumor cells can be precisely recognized by the AS1411 aptamer encoded in the template strand of DNA, giving DOX/HRP-DFs the ability to identify

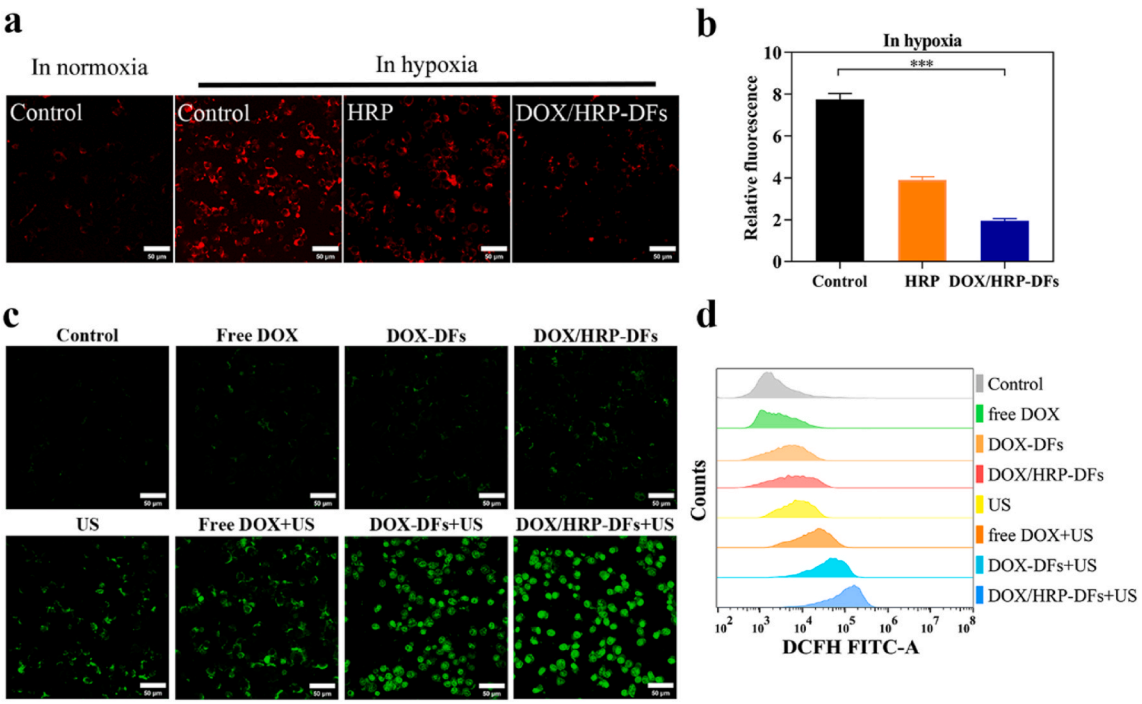

Fig. 3. Intracellular oxygen content and ROS production assessment. (a) and (b). CLSM images of intracellular oxygen levels of hypoxic LLC cells *in vitro* after different treatments (a) and relative fluorescence against the control in normoxia (b), scale bar = 50 μm. (c) CLSM images of intracellular ROS generation after different treatments, scale bar = 50 μm. (d) Flow cytometric analysis of intracellular ROS generation after different treatments. ***$P < 0.001$.

tumors. LLC cells (high nucleolin expressing) and 16HBE cells (low nucleolin expressing) were used to evaluate whether DOX/HRP-DFs could specifically target tumor cells. Results from CLSM and flow cytometry revealed that LLC cells fluoresced more intensely than 16HBE cells after being incubated with FITC-DOX/HRP-DFs (with FITC fluorescent labeling and AS1411 sequence) for 4 h, indicating that DOX/HRP-DFs possesses effective tumor targeting properties (Fig. 4a and b). To further analyze the internalization pathway of DOX/HRP-DFs into LLC cells, lysosomes were stained with lysotracker and the co-localization of lysosomes with DOX/HRP-DFs was monitored. CLSM results showed that DOX/HRP-DFs (the red fluorescent) and lysosomes (the green fluorescent) were mostly co-located after 4 h incubation, demonstrating that DOX/HRP-DFs were specifically taken up by LLC cells through endocytosis (Fig. 4e).

In addition, to evaluate AS1411-mediated tumor uptake, the AS1411 sequence in the DNA template was replaced with a random sequence to prepare non-targeted nanoflowers (FITC-DOX/HRP-NADFs). The experimental results showed that the fluorescence intensity of LLC cells incubated with the FITC-DOX/HRP-NADFs was significantly lower compared to FITC-DOX/HRP-DFs, indicating that the AS1411 aptamer is effective in promoting DOX/HRP-DFs tumor targeting and enhancing cell uptake through specific recognition mediated by nucleolin (Fig. 4c and d).

3.8. *In vitro* cytotoxicity

The *in vitro* antitumor effects of DOX/HRP-DFs were investigated by CCK-8 assay. In normoxic cells, free DOX, DOX-DFs and DOX/HRP-DFs all showed dose-dependent cytotoxicity to LLC cells and the survival rates of LLC cells at the highest concentrations were 39.45 ± 0.81%, 35.4 ± 1.06% and 34.35 ± 2.15%, respectively, owing to the ability of DOX-DFs and DOX/HRP-DFs to target LLC cells and achieve drug release control, which effectively increased the intracellular drug concentration (Fig. S6a). However, in hypoxic environment, the cytotoxicity of free DOX (cell viability 68.78 ± 1.71%) was significantly inhibited, while DOX-DFs and DOX/HRP-DFs still had higher cytotoxicity, with cell viability of 53.07 ± 2.09% and 45.88 ± 1.06%, respectively (Fig. S6b). The capacity of DOX/HRP-DFs to catalyze intracellular H_2O_2 synthesis of O_2 while accurately delivering medicines, which greatly reduced tumor hypoxia and enhanced the cell-killing power, caused them to demonstrate the highest cytotoxicity among the groups. Furthermore, the antitumor effects of different drugs combined with US were evaluated under normoxia and hypoxia (Fig. 5a and b). The cytotoxicity of free DOX and DOX-DFs combined US was significantly reduced in hypoxic cells when compared to normoxic conditions. However, DOX/HRP-DFs combined US could dramatically lower the IC_{50} value of tumor cells and successfully increase the cytotoxicity of DOX on LLC cells cultivated *in vitro* (Table S4), demonstrating that the DOX/HRP-DFs created in this study could improve the therapeutic effect of SDT on tumor cells.

After being subjected to various treatments, LLC cells were stained with PI (red fluorescence) and Calcein-AM (green fluorescence), followed by CLSM observation, wherein green fluorescence indicates that the cells are alive and red fluorescence indicates that the cells are dead. Fig. 5c illustrates how LLC cells treated with DOX/HRP-DFs had intense red fluorescence, indicating strong cytotoxicity of DOX/HRP-DFs, while LLC cells treated with free DOX and DOX-DFs showed obvious green fluorescence and weak red fluorescence, indicating that there were more surviving cells. After ultrasound irradiation, the red fluorescence of each group was significantly enhanced, among which only a small amount of green fluorescence existed in LLC cells treated with DOX/HRP-DFs combined US, proving that DOX/HRP-DFs combined US has powerful cytotoxic ability.

3.9. *In vitro* apoptosis assay

To verify the ability of DOX/HRP-DFs combined US in inducing cell apoptosis, cells were double-stained by Annexin V-FITC and DAPI, and then flow cytometry was used to detect the apoptosis rate of cells (Fig. 5d). In line with the findings of the CLSM, DOX/HRP-DFs showed the highest apoptosis rate among the drug related-only group. In addition, after ultrasound irradiation, the apoptosis rate of cells after DOX/HRP-DFs treatment was 72.36 ± 1.60%, which was significantly higher

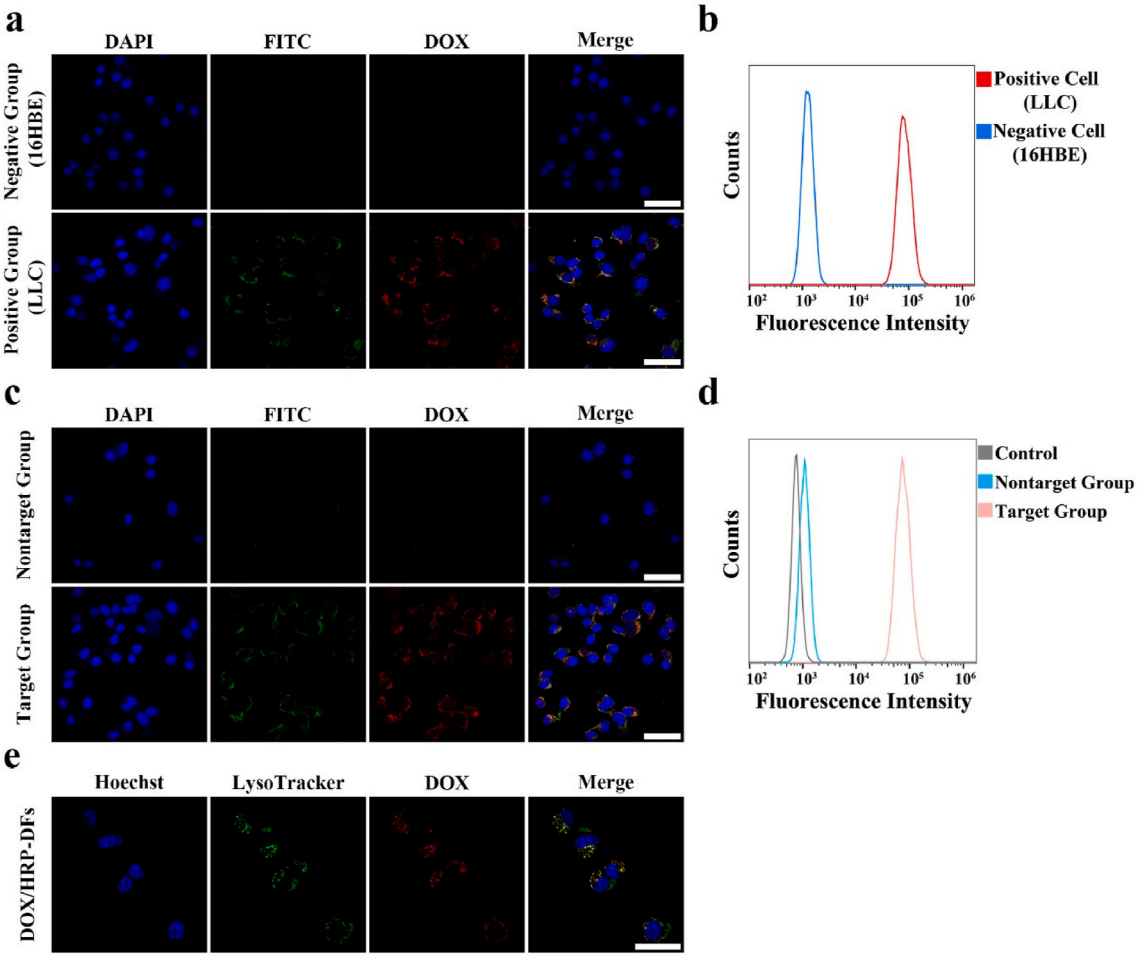

Fig. 4. DNA aptamer-mediated specific cancer cell recognition *in vitro*. (a) and (b). CLSM images (a) and flow cytometric analysis (b) of LLC cell and 16HBE cell treated with DOX/HRP-DFs, scale bar = 50 μm. (c) and (d). CLSM images (c) and flow cytometric analysis (d) of LLC cell treated with DOX/HRP-NADFs and DOX/HRP-DFs, scale bar = 50 μm. (e) CLSM images of subcellular localization of DOX/HRP-DFs in LLC cells, scale bar = 50 μm.

than that of DOX-DFs and free DOX. The experimental findings demonstrated that DOX/HRP-DFs could still induce apoptosis of LLC cells under hypoxia, while significantly increasing the killing ability of SDT on LLC cells.

Then, the expression of apoptosis pathway-related proteins Bax and Bcl-2 was detected using Western blotting analysis (Fig. 5g). Compared with free DOX and DOX-DFs, the expression of Bcl-2 was decreased and the expression of Bax was increased in LLC cells treated with DOX/HRP-DFs. Similarly, LLC cells treated with DOX/HRP-DFs showed the same situation after ultrasonic irradiation, which again confirmed the ability of DOX/HRP-DFs to significantly promote tumor cell apoptosis.

3.10. *In vitro migration and invasion ability of LLC cells*

The inhibition of DOX/HRP-DFs on LLC cell migration was examined by a scratch assay. As shown in fig. 5e and S7, the scratch healing rate of free DOX group was 28.45 ± 1.79%, while that of DOX-DFs group and DOX/HRP-DFs group showed a decrease of 18.73 ± 0.91% and 12.96 ± 1.33%, respectively ($P < 0.001$). However, when different drugs were combined US for treatment, the scratch healing ratio of cells in each experimental group significantly reduced, with the lowest scratch healing rate of 4.14 ± 1.40% in DOX/HRP-DFs group ($P < 0.001$). The experimental results demonstrated that DOX/HRP-DFs in combination with US could effectively inhibit the migration ability of LLC cells. This study further investigated the inhibitory effect of LLC cells treated with DOX/HRP-DFs on invasion ability which was measured by the number of cells penetrating the membrane. When compared to free DOX and DOX-DFs (both $P < 0.001$), LLC cells treated with DOX/HRP-DFs had the lowest number of cells (194.3 ± 37.6 cells) to penetrate the membrane. The findings are presented in fig. 5f and S8. Moreover, the number of cell penetrations in each treatment group significantly decreased when cells were treated with a drug and US combination, with only 102.0 ± 17.3 cells in the DOX/HRP-DFs combined US group ($P < 0.001$). This investigation demonstrated that DOX/HRP-DFs with US had a powerful inhibitory effect on the invasion ability of LLC cells.

3.11. *In vivo tumor-targeting ability and biodistribution of DOX/HRP-DFs*

To verify the *in vivo* tumor targeting ability of DOX/HRP-DFs, Cy5.5-DOX/HRP-DFs and Cy5.5-DOX/HRP-NADFs were injected into LLC tumor-bearing mice via the tail vein respectively, and fluorescence images were taken at different time points and the corresponding fluorescence intensity was recorded. As shown in Fig. 6a and b, the fluorescence intensity at the tumor site of mice in the targeted group increased with the extension of time and peaked at 24 h post-injection, and the fluorescence remained *in vivo* 48 h after injection, while the fluorescence intensity of the tumor in the non-targeted group was always lower than that in the targeted group. Subsequently, the distribution of DOX/HRP-DFs and DOX/HRP-NADFs in tumor tissues (in which co-localization of DOX with the red fluorescence is observable) at 24 h after injection was observed by CLSM (Fig. 6e and f). The results showed that the red fluorescence inside the tumor tissues was

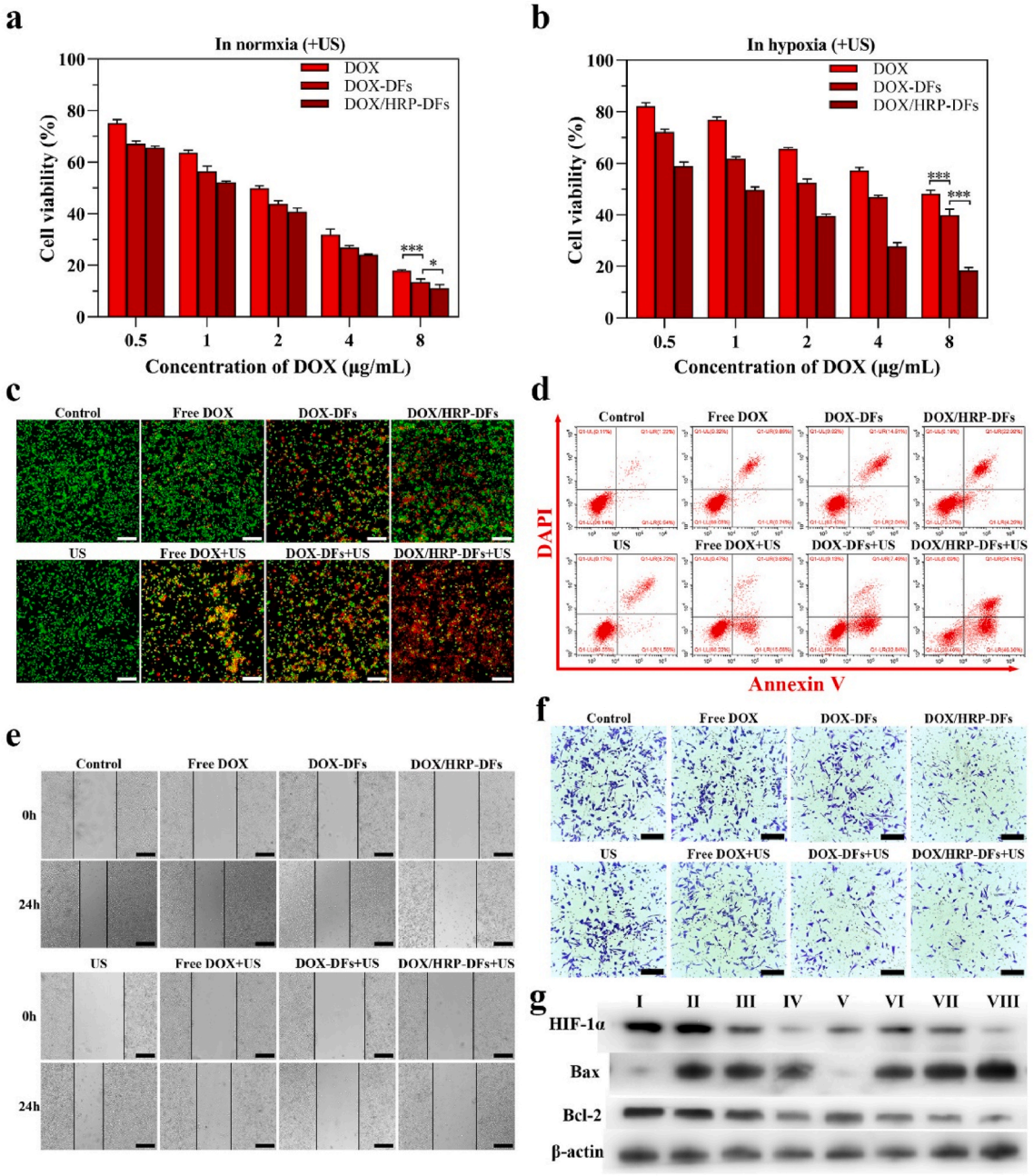

Fig. 5. *In vitro* cytotoxicity of free DOX, DOX-DFs and DOX/HRP-DFs combined with US on LLC cells under normoxic (a) and hypoxic conditions (b). (c). CLSM images showed apoptosis of LLC cells after different treatments, scale bar = 100 μm. (d). Flow cytometric analysis apoptosis of LLC cell induced by different treatments. (e). Scratch test showed that DOX/HRP-DFs combined US inhibited LLC cell migration, scale bar = 300 μm. (f). Transwell assay shows the ability of DOX/HRP-DFs combined US to inhibit the invasion of LLC cells, scale bar = 200 μm*$P < 0.05$, ***$P < 0.001$. (g). HIF-1α, Bax and Bcl-2 levels of LLC cells were analyzed by Western blotting. The cells are separately treated with PBS (control) (I); free DOX (II); DOX-DFs (III); DOX/HRP-DFs (IV); US (V); free DOX + US (VI); DOX-DFs + US (VII); and DOX/HRP-DFs + US (VIII).

significantly higher in the targeting group than that in the nontargeting group, demonstrating that DOX/HRP-DFs could maintain excellent targeting ability *in vivo*.

In addition, the main organs (heart, liver, spleen, lung, and kidney) and tumor tissues of tumor bearing mice were collected separately for *ex vivo* fluorescence imaging to evaluate the *in vivo* distribution of DOX/HRP-DFs. As shown in Fig. 6c and d, DOX/HRP-DFs were mainly distributed to tumor, liver and kidney sites after 48 h post-injection, which proved that DOX/HRP-DFs were mainly taken up by the endothelial reticular system and then cleared. This experiment showed that DOX/HRP-DFs have advantages in targeting as well as retention properties *in vivo*.

3.12. Evaluation of antitumor effect in vivo

The anti-tumor effects of DOX/HRP-DFs were investigated *in vivo* by LLC tumor bearing C57BL/6 mouse model. During an observation period of 14 days, the body weight and tumor volume of mice in each treatment group were recorded every two days, and these results was shown in fig. 7b and c and S9. The final tumor volume was 1107.08 ± 135.28 mm^3 for free DOX treatment. Nevertheless, the tumor volumes of mice treated with DOX-DFs and DOX/HRP-DFs increased more slowly, with the volumes at the end of treatment being 822.63 ± 63.83 mm^3 and 641.10 ± 109.15 mm^3, respectively. This was inextricably associated with the *in vivo* targeting and oxygen generation properties of DOX/HRP-DFs.

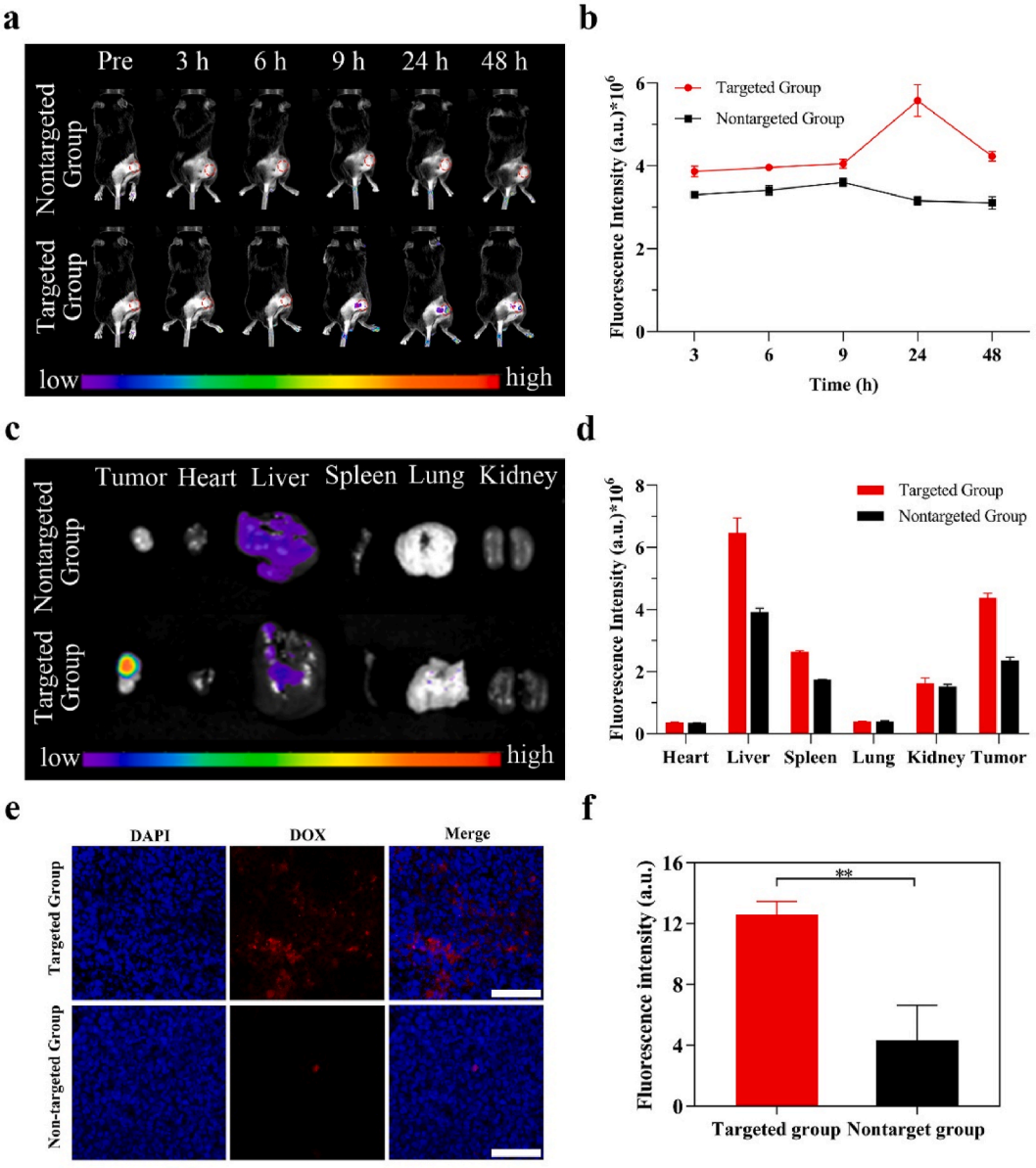

Fig. 6. *In vivo* DOX/HRP-DFs tumor-targeting ability and biodistribution. (a). Fluorescence images of C57BL/6 tumor-bearing mice at different time points (3 h, 6 h, 9 h, 24 h, 48 h) after injection of Cy5.5-labeled DOX/HRP-DFs and Cy5.5-labeled DOX/HRP-NADFs. (b). Fluorescence intensity of tumor tissue at different time points. (c). Fluorescence imaging of *ex vivo* tumor tissues and major organs at 48 h after Cy5.5-labeled DNA nanoflowers injection. (d). Fluorescence intensity *ex vivo* tumor tissues and major organs at 48 h after Cy5.5-labeled DNA nanoflowers injection, scale bar = 50 μm. (e) and (f). CLSM images (e) and fluorescence intensity (f) of tumor frozen section at 24 h post-injection of Cy5.5-labeled DNA nanoflower, scale bar = 200 μm ** represents $P < 0.01$.

Compared to employing free drugs or nanoparticles alone, the therapeutic effect of using drugs or nanoparticles in conjunction with US therapy was greater. Of these, the tumor growth of mice treated with DOX/HRP-DFs combined US was most obviously inhibited in comparison to other experimental groups, and the final tumor volume was only 236.71 ± 38.90 mm^3. In addition, mice in each treatment group gained weight during the treatment. What's more, the survival curve data indicated that mice treated with DOX/HRP-DFs in conjunction with US had much longer survival times, with a survival rate of 80% even after 60 days (Fig. 7d).

The pathological alterations of the tumor tissues were then evaluated using hematoxylin-eosin (H&E) staining, and TUNEL immunofluorescence assays were used to measure the amount of apoptosis in the tumor tissues in response to various therapies. Fig. 7e shows that H&E staining of tumor cells following DOX/HRP-DFs combined US therapy showed cellular structural changes with necrosis and nucleus fragmentation in comparison to the control group. In contrast, TUNEL fluorescence labeling revealed the most intense green fluorescence in the tumor tissue after DOX/HRP-DFs combined US therapy compared to other treatment groups, consistent with the H&E staining results, demonstrating that significant numbers of tumor cells displayed apoptosis (fig. 7f and S10). The findings from H&E staining and the TUNEL assay supported that DOX/HRP-DFs combined US had notable anti-tumor effect.

In addition, the level of oxidative damage was indirectly determined by measuring the level of malondialdehyde (MDA) in the tumor tissues of each treatment group (Fig. S14). The experimental results showed that the MDA level was significantly higher in each treatment group after ultrasound irradiation than in the group treated with drugs alone, and the oxidative damage level was higher in the tumor tissues treated with DOX/HRP-DFs, compared with free DOX and DOX-DFs, which proved that increased oxygen content could effectively increase ROS production in tumor tissues.

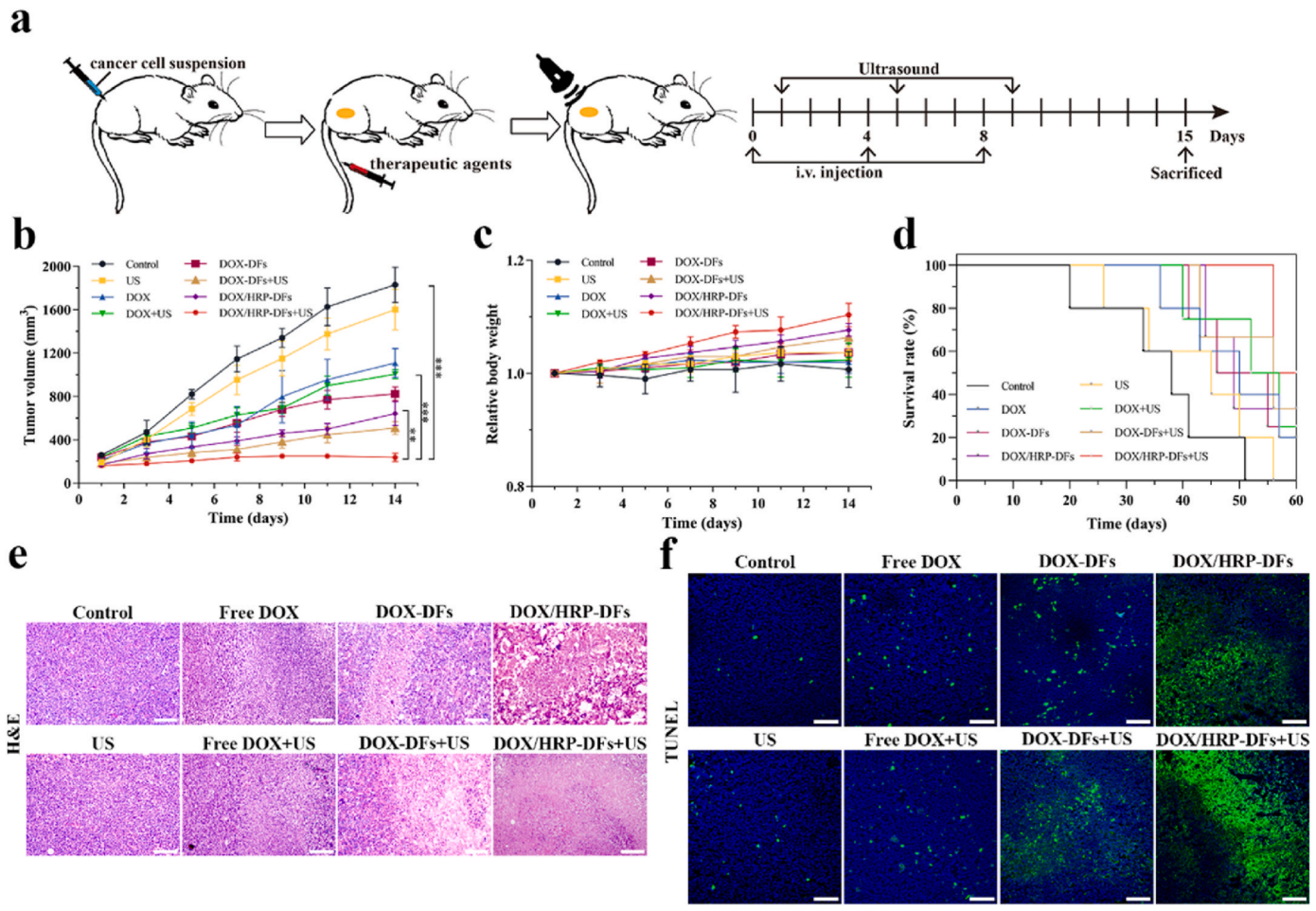

Fig. 7. Evaluation of antitumor effect *in vivo*. (a). The illustration of the treatment in C57BL/6 LLC tumor-bearing mice. Tumor volumes (b), relative body weight (c) and survival curve (d) of tumor-bearing mice in each treatment group after 14 days of different treatments. (e). Representative H&E staining images of the tumor tissues in tumor-bearing mice with different treatments, scale bar = 100 μm. (f). TUNEL fluorescence staining of tumor tissues in each treatment group after 14 days of different treatments, scale bar = 150 μm $^{**}P < 0.01$, $^{***}P < 0.001$.

HIF-1α upregulates vascular endothelial growth factor (VEGF), which in turn encourages neovascularization, when present in the hypoxic microenvironment of tumor tissues. Tumor tissues from each treatment group were subjected to immunohistochemical labeling for HIF-1α, VEGF, and CD31 to investigate the potential effects of DOX/HRP-DFs combined US on enhancing hypoxia and reducing neovascularization in tumor tissues. The number of positive cells in the HIF-1α, VEGF, and CD31 labeling of tumor tissues treated with DOX/HRP-DFs combined US was dramatically reduced when compared to other treatment groups, as shown in (Fig. 8a, b and 8c). Meanwhile, the serum ELISA results of each treatment group also confirmed that DOX/HRP-DFs combined US treatment effectively reduced the levels of HIF-1α, VEGF and CD31 in tumor serum (Fig. 8d, e and 8f). This is due to the capacity of HRP encapsulated in DOX/HRP-DFs to effectively catalyze intracellular H_2O_2 to generate O_2 to alleviate tumor tissue hypoxia.

3.13. *In vivo* biosafety of DOX/HRP-DFs

The *in vivo* biosafety of DOX/HRP-DFs was evaluated by blood biochemical indexes and histopathology of vital organs. And the blood biochemical test results showed that the liver function indexes, such as alanine aminotransferase (ALT), aspartate aminotransferase (AST) and total bilirubin (TBIL), renal function indexes, such as creatinine (CREA) and blood urea nitrogen (BUN) and cardiac function indexes, such as kinase (CK), were all within the normal range and did no differ significantly from the control group ($P < 0.05$), indicating that DOX/HRP-DFs was not toxic to C57BL/6 mice at a certain dose (Fig. S11). In addition, since DOX/HRP-DFs formulation needs to be transported through blood, hemolysis tests are important to detect the biosafety of DOX/HRP-DFs *in vivo*. The results showed that no significant hemolysis was observed when the red blood cells suspension was co-incubated with different concentrations of DOX/HRP-DFs (DOX with final concentration of 2, 4, 8, 16, 32 and 64 μg/mL), and the hemolysis rate was less than 5%, which proved that DOX/HRP-DFs had good biocompatibility (Fig. S12). The finding by H&E pathological staining after 14 days of therapy that there was no obvious coagulation necrosis and injury in the heart, liver, spleen, lung, kidney, and other major organs of C57BL/6 mice with DOX/HRP-DFs treatment further supported the biological safety of DOX/HRP-DFs *in vivo* (Fig. S13).

3.14. *Activation of immune response mediated by CG sequence in DOX/HRP-DFs*

The activation of immune response by CG sequence was reflected by detecting the level of serum cytokines in mice (Fig. S15). Serum ELISA results showed that IFN-γ, TNF-α, and IL-6 levels were relatively increased in the DOX/HRP-DFs group, implying that CG sequences rich in DOX/HRP-DFs can induce the production of serum immune factors and have certain immunostimulatory effects.

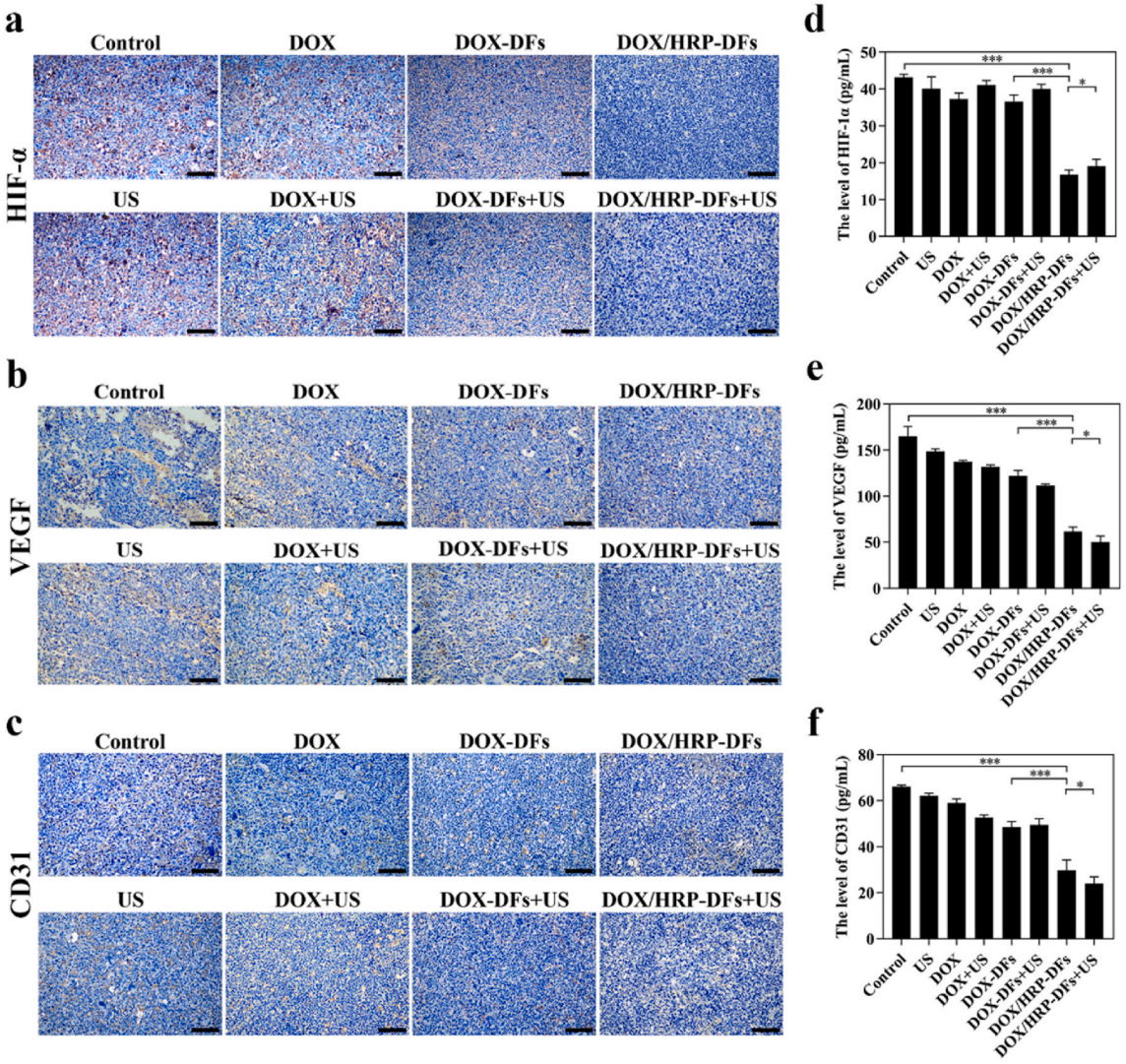

Fig. 8. *In vivo* improvement of tumor hypoxia and angiogenesis. HIF-1α (a), VEGF (b) and CD31 (c) immunohistochemical staining of tumor tissues and the serum level of HIF-1α (d), VEGF (e) and CD31 (f) in each treatment group after 14 days of different treatments, scale bar = 100 μm $^{*}P < 0.05$, $^{***}P < 0.001$.

4. Discussion

Currently, chemotherapy remains the main treatment option for lung cancer in clinical practice [42]. However, conventional chemotherapeutic drugs are non-selectively targeted, lack controlled administration in clinical treatment, and cannot be effectively accumulated in tumors. Chemotherapy-induced systemic toxicity has become a pressing challenge in clinical treatment [43,44]. Furthermore, it is widely known that hypoxic microenvironments found in solid tumors are one of the major contributors of drug resistance [45–47].Thus, our research has developed a multifunctional DNA nanoflowers drug delivery platform that can avoid these tissues and specifically target cancer cells. By lowering hypoxia in the tumor tissue, this drug delivery platform can enhance the therapeutic efficacy of chemotherapy when applied in conjunction with SDT for metastatic lung cancer.

The RCA, an enzyme reaction, which amplifies single stranded DNA effectively under isothermal conditions, is commonly employed to increase detection signals with good stability. When magnesium pyrophosphate is present as a co-precipitant during the nanoflower formation process, long RCA products have been demonstrated to spontaneously self-assemble into densely packed DNA-inorganic hybrid nanoflower structures. Using RCA technology, cell-targeting groups, aptamers, fluorophores, and drug-loading sequences can be added to multifunctional DNA nanoflowers [48–50].After that, these DNA nanoflowers can be utilized for bioimaging, bioassays, and drug delivery. In the present study, we successfully synthesized DNA nanoflowers loaded with DOX and HRP catalytic enzyme (DOX/HRP-DFs) by RCA technique. The DOX/HRP-DFs were observed by SEM and TEM in a lamellar flower-like porous structure, which provides the possibility of physical encapsulation of the drug (Fig. 1d and e). The stability of DOX/HRP-DFs was also investigated in this experiment, and the results showed that DOX/HRP-DFs had high serum stability and anti-enzymatic ability, which was inseparable from the dense structure of DOX/HRP-DFs and also laid the foundation for the subsequent *in vivo* experiments of DOX/HRP-DFs (Fig. 2a).

Due to the programmability of DNA nanoflowers, DOX was able to non-covalently bind to double-stranded DNA through intercalation into the helix, and the amount of drug loading was regulated by encoding a drug loading sequence in the DNA template strand of DOX/HRP-DFs [14,51]. The DOX/HRP-DFs designed in this work have an extremely high drug loading rate of 73.03 ± 3.8%. Among these, it was determined that 42.10 ± 1.97% of the DOX was loaded into drug binding sequences of DNA nanoflowers through intercalation, while the remaining DOX was speculated to be physically encapsulated into the DOX/HRP-DFs. Fig. 2b presents these results. Compared to nanoparticles made from other materials, the nanoflowers created in this study had a substantially

higher drug loading rate. For instance, the PLGA nanoparticle's drug loading rate is frequently less than 10%. Good therapeutic effect of DOX/HRP-DFs was guaranteed by the high drug loading rate. The AS1411 aptamer sequence, which binds with nucleolin expressed on cancer cell surfaces to specifically transport drugs to tumor cells, was also embedded in the DNA template strand of DOX/HRP-DFs [52,53]. Through the results of flow cytometry and CLSM, it was found, as shown in Fig. 4, that DOX/HRP-DFs specifically attached to LLC cells that are nucleolin-highly expressed and was further taken up by the cell via lysosome-mediated endocytosis.

A weak acid environment is one of the primary characteristics of solid tumor. The pH-responsive drug release of DOX/HRP-DFs was confirmed by our research. At pH 5.5, their 48h drug release rate could exceed 80%, whereas in physiological buffer (pH = 7.4), it was considerably retarded (Fig. 2c). The magnesium pyrophosphate core's automatic disintegration in an acidic environment led to drug DOX releasing. DOX/HRP-DFs structure collapse in an acidic environment (pH = 5.5) can be observed from Fig. S4. DOX is released from nanoparticles that stay in the body for a long period under acidic conditions in tumor tissue; this can lessen the damaging effects of DOX on normal tissues. The release of DOX from nanoparticles that remain in tumor tissues for an extended period of time under acidic conditions can mitigate the deleterious effects on normal tissues.

Hypoxia in tumor tissues is a significant factor in the development of their enhanced drug resistance, which has a negative impact on the efficacy of tumor therapy. HRP encapsulated in DOX/HRP-DFs can effectively catalyze the decomposition of H_2O_2 to generate O_2. The capacity of DOX/HRP-DFs to produce oxygen was examined in this study, and the results demonstrated that DOX/HRP-DFs could catalyze H_2O_2 to produce O_2, and they produced more oxygen than free HRP (Fig. 2f and g). This might be the secondary structure of HRP was altered by the negatively charged environment of DNA nanoflowers, considerably improving its catalytic efficacy [54,55].

Subsequently, intracellular hypoxic of LLC cells relief was investigated by an oxygen detection probe $[(Ru(dpp)_3)]Cl_2$ probe, with the degree of intracellular hypoxia being positively correlated with the intensity of red fluorescence (Fig. 3a and b). Additionally, hypoxia inducible factor-1alpha (HIF-1α) is a marker for hypoxic conditions. By using immunohistochemistry labeling for HIF-1α expression, hypoxic tumor regions were also investigated. When compared to US alone or DOX-DFs, the levels of HIF-1α in tissues revealed that DOX/HRP-DFs with US irradiation may considerably boost tumor hypoxia alleviation (Fig. 8a). The serum HIF-1α ELISA results were consistent with the immunohistochemistry investigation (Fig. 8d). The aforementioned characteristics of DOX/HRP-DFs enable them to precisely target tumor cells, release drugs efficiently in response to the tumor's acidic environment, and alleviate the hypoxic conditions inside tumor cells. Furthermore, the physical penetration of ultrasound made it possible for more DOX/HRP-DFs to penetrate the target region, which released more HRP and alleviated tissue hypoxia.

This experiment investigated the inhibitory effects of DOX/HRP-DFs combined with US on LLC lung cancer cells both *in vitro* and *in vivo*. According to Table S4, DOX/HRP-DFs combined US could dramatically lower the IC_{50} value of tumor cells and successfully increase the cytotoxicity of DOX on LLC cells cultivated *in vitro*, demonstrating that the DOX/HRP-DFs created in this work could improve the therapeutic effect of SDT on tumor cells. In addition, this study also evaluated the therapeutic effect of DOX/HRP-DFs combined US on LLC tumor-bearing mice, and the experimental results showed that DOX/HRP-DFs combined US in this study could effectively inhibit volume growth of tumor in comparison to other experimental groups(fig. 7b and S8). What's more, the histopathology confirmed that tumor tissue suffered necrosis and nuclear fragmentation during therapy, and meanwhile, TUNEL fluorescence staining results demonstrated that DOX/HRP-DFs combined US significantly boosted apoptosis in tumor cells (Fig. 7e and f).

Tumor tissues under hypoxia state have increased the expression of HIF-1α, subsequently leading to upregulated VEGF expression and abnormal tumor angiogenesis [56–58]. Additionally, CD31, a member of the immunoglobulin superfamily, is widely utilized to evaluate tumor angiogenesis by counting CD31 positive cells to estimate the amount of tumor microvessels [59]. In order to achieve a better drug delivering to tumor cells, DOX/HRP-DFs may reduce tumor tissues' hypoxic environments, which would inhibit the expression of VEGF and CD31 and restore tumor angiogenesis. The immunohistochemical staining and ELISA results revealed that, compared to the other treatment group, DOX/HRP-DFs decreased the expression of HIF-1α, VEGF, and CD31 in LLC lung cancer tissues (Fig. 8a, b and 8c). These results again demonstrated that the prepared DOX/HRP-DFs have an ability to efficiently deliver and specifically target tumor cells, substantially alleviate tumor hypoxia to enhance SDT efficacy and achieve significant tumor suppression.

The mechanical effects of ultrasound may affect the physiological activity of cells, causing structural changes and the thermal effects may also cause damage to cells, but more importantly, ultrasound can activate sonosensitizers to produce highly lethal ROS, which has substantial anti-tumor effects, marvelous tissue penetration and non-invasiveness properties. In addition to being a chemotherapy medication to treat various cancers, DOX is also one of the most well-known and potent sonosensitizers [40]. After combining with ultrasound, it exhibits a SDT effect. In the present study, higher levels of ROS were detected in the DOX/HRP-DFs formulations following ultrasound activation (fig. 3c and d and S14), indicating that ultrasound can activate DOX to increase more ROS content, which in turn heightens the anti-tumor activity. Through a rapid O_2 release and an increase in blood perfusion, DOX/HRP-DFs were able to alleviate hypoxia and promote ROS generation under the influence of ultrasonic irradiation, which enhanced the anticancer activity of SDT.

Inhibition of tumor metastasis is also a more important aspect of tumor therapy, so this experiment also explored the potential of DOX/HRP-DFs combined with US to inhibit tumor cell metastasis. *In vitro* experiments show that DOX/HRP-DFs combined with ultrasound has the potential to inhibit the migration and invasion of tumor cells, and the inhibitory effect of chemo-sonodynamic therapy is greater than that of chemotherapy alone (Fig. 5e and f). Further *in vivo* experiments show that DOX/HRP-DFs can effectively alleviate tumor hypoxia and down-regulate HIF-1α expression, and after combined US, it could further down-regulate the level of VEGF and CD31 and improve the vascular supply of tumor tissue, which is also a possible mechanism for DOX/HRP-DFs combined with ultrasound to inhibit tumor metastasis.

According to the aforementioned findings, DOX/HRP-DFs combined US provides the optional tumor-suppression effect through a variety of synergistic mechanisms, such as the following: 1. the capacity to specifically target tumors; 2. oxygenation to alleviate tumor hypoxia, normalize tumor angiogenesis, and reverse hypoxia-induced tumor drug resistance; 3. reducing the inhibitory effect of hypoxia on SDT, increasing ROS production, and improving the therapeutic effect of SDT combined with chemotherapy on tumors.

5. Conclusion

In this study, we successfully prepared a multifunctional DNA nanoflowers drug delivery platform (DOX/HRP-DFs) which is co-loaded with DOX and HRP, and it performs satisfactorily in terms of both total drug loading rate and drug loading performance. The DOX/HRP-DFs exhibited remarkable tumor targeting ability both *in vivo* and *in vitro*, and they could effectively increase the drug concentration in tumor cells while minimizing the toxic side effects. DOX/HRP-DFs combined with US could significantly ameliorate the hypoxia of tumor tissues, reducing the development of tumor aberrant blood vessels by accelerating the production of oxygen from hydrogen peroxide in tissues and subsequently down-regulating cytokines including HIF-1α, VEGF and CD31. Under ultrasonic irradiation, the multifunctional DNA nanoflowers were

able to produce notable amounts of reactive oxygen species both *in vitro* and *in vivo*, and significantly inhibited the growth of tumor cells. Our research demonstrates that the multifunctional DNA nanoflowers drug delivery platform developed in this study is anticipated to offer a promising strategy for the treatment of metastatic lung cancer.

Declarations

5.1. Ethics approval and consent to participate

This study complied with the ethical standards established by the Experimental Animal Ethics Committee of Chongqing Medical University (Ethical Number: 2,022,152).

Funding

This research did not receive any specific grant from funding agencies in the public, commercial, or not-for-profit sectors.

CRediT authorship contribution statement

Hongjian Liao: Writing – original draft, Methodology, Formal analysis, Data curation, Conceptualization. **Yuchao Cao:** Software, Investigation, Data curation. **Can Hu:** Investigation. **Shangfeng Shen:** Investigation. **Zhifei Zhang:** Investigation, Conceptualization. **Dairong Li:** Writing – review & editing, Supervision. **Yonghong Du:** Supervision, Project administration.

Declaration of competing interest

The authors declare that they have no known competing financial interests or personal relationships that could have appeared to influence the work reported in this paper.

Data availability

Data will be made available on request.

Acknowledgements

Not applicable.

Appendix A. Supplementary data

Supplementary data to this article can be found online at https://doi.org/10.1016/j.mtbio.2024.101005.

References

[1] R.L. Siegel, K.D. Miller, A. Jemal, Cancer statistics, 2020, CA, Cancer J. Clin. 70 (2020) 7–30, https://doi.org/10.3322/caac.21590.
[2] F. Nasim, B.F. Sabath, G.A. Eapen, Lung cancer, Med. Clin. 103 (2019) 463–473, https://doi.org/10.1016/j.mcna.2018.12.006.
[3] Y. Lv, R. Liu, S. Xie, X. Zheng, J. Mao, Y. Cai, W. Chen, Calcein-acetoxymethy ester enhances the antitumor effects of doxorubicin in nonsmall cell lung cancer by regulating the TopBP1/p53RR pathway, Anti Cancer Drugs 28 (2017) 861–868, https://doi.org/10.1097/CAD.0000000000000527.
[4] K. Kuerban, X. Gao, H. Zhang, J. Liu, M. Dong, L. Wu, R. Ye, M. Feng, L. Ye, Doxorubicin-loaded bacterial outer-membrane vesicles exert enhanced anti-tumor efficacy in non-small-cell lung cancer, Acta Pharm. Sin. B 10 (2020) 1534–1548, https://doi.org/10.1016/j.apsb.2020.02.002.
[5] Z. Dai, X.-Z. Song, J. Cao, Y. He, W. Wen, X. Xu, Z. Tan, Dual-stimuli-responsive TiO x/DOX nanodrug system for lung cancer synergistic therapy, RSC Adv. 8 (2018) 21975–21984, https://doi.org/10.1039/c8ra02899k.
[6] X.-Q. Dou, H. Wang, J. Zhang, F. Wang, G.-L. Xu, C.-C. Xu, H.-H. Xu, S.-S. Xiang, J. Fu, H.-F. Song, Aptamer-drug conjugate: targeted delivery of doxorubicin in a HER3 aptamer-functionalized liposomal delivery system reduces cardiotoxicity, Int. J. Nanomedicine 13 (2018) 763–776, https://doi.org/10.2147/IJN.S149887.
[7] O. Tacar, P. Sriamornsak, C.R. Dass, Doxorubicin: an update on anticancer molecular action, toxicity and novel drug delivery systems, J. Pharm. Pharmacol. 65 (2013) 157–170, https://doi.org/10.1111/j.2042-7158.2012.01567.x.
[8] L. Lv, X. An, H. Li, L. Ma, Effect of miR-155 knockdown on the reversal of doxorubicin resistance in human lung cancer A549/dox cells, Oncol. Lett. 11 (2016) 1161–1166, https://doi.org/10.3892/ol.2015.3995.
[9] H.-H. Chen, I.-L. Lu, T.-I. Liu, Y.-C. Tsai, W.-H. Chiang, S.-C. Lin, H.-C. Chiu, Indocyanine green/doxorubicin-encapsulated functionalized nanoparticles for effective combination therapy against human MDR breast cancer, Colloids Surf. B Biointerfaces 177 (2019) 294–305, https://doi.org/10.1016/j.colsurfb.2019.02.001.
[10] C. Cao, Q. Wang, Y. Liu, Lung cancer combination therapy: doxorubicin and β-elemene co-loaded, pH-sensitive nanostructured lipid carriers, Drug Des. Dev. Ther. 13 (2019) 1087–1098, https://doi.org/10.2147/DDDT.S198003.
[11] Y. Hong, S. Che, B. Hui, Y. Yang, X. Wang, X. Zhang, Y. Qiang, H. Ma, Lung cancer therapy using doxorubicin and curcumin combination: targeted prodrug based, pH sensitive nanomedicine, Biomed. Pharmacother. Biomedecine Pharmacother. 112 (2019) 108614, https://doi.org/10.1016/j.biopha.2019.108614.
[12] S. Nummelin, J. Kommeri, M.A. Kostiainen, V. Linko, Evolution of structural DNA nanotechnology, Adv. Mater. Deerfield Beach Fla. 30 (2018) e1703721, https://doi.org/10.1002/adma.201703721.
[13] G. Zhu, R. Hu, Z. Zhao, Z. Chen, X. Zhang, W. Tan, Noncanonical self-assembly of multifunctional DNA nanoflowers for biomedical applications, J. Am. Chem. Soc. 135 (2013) 16438–16445, https://doi.org/10.1021/ja406115e.
[14] Y. Yuan, Z. Gu, C. Yao, D. Luo, D. Yang, Nucleic acid-based functional nanomaterials as advanced cancer therapeutics, Small Weinh. Bergstr. Ger. 15 (2019) e1900172, https://doi.org/10.1002/smll.201900172.
[15] Y. Dong, C. Yao, Y. Zhu, L. Yang, D. Luo, D. Yang, DNA functional materials assembled from branched DNA: design, synthesis, and applications, Chem. Rev. 120 (2020) 9420–9481, https://doi.org/10.1021/acs.chemrev.0c00294.
[16] Q. Hu, H. Li, L. Wang, H. Gu, C. Fan, DNA nanotechnology-enabled drug delivery systems, Chem. Rev. 119 (2019) 6459–6506, https://doi.org/10.1021/acs.chemrev.7b00663.
[17] Y. Hu, C.M. Niemeyer, From DNA nanotechnology to material systems engineering, Adv. Mater. Deerfield Beach Fla. 31 (2019) e1806294, https://doi.org/10.1002/adma.201806294.
[18] X. Guo, F. Li, L. Bai, W. Yu, X. Zhang, Y. Zhu, D. Yang, Gene circuit compartment on nanointerface facilitatating cascade gene expression, J. Am. Chem. Soc. 141 (2019) 19171–19177, https://doi.org/10.1021/jacs.9b11407.
[19] R. Hu, X. Zhang, Z. Zhao, G. Zhu, T. Chen, T. Fu, W. Tan, DNA nanoflowers for multiplexed cellular imaging and traceable targeted drug delivery, Angew. Chem. Int. Ed Engl. 53 (2014) 5821–5826, https://doi.org/10.1002/anie.201400323.
[20] L. Zhang, R. Abdullah, X. Hu, H. Bai, H. Fan, L. He, H. Liang, J. Zou, Y. Liu, Y. Sun, X. Zhang, W. Tan, Engineering of bioinspired, size-controllable, self-degradable cancer-targeting DNA nanoflowers via the incorporation of an artificial sandwich base, J. Am. Chem. Soc. 141 (2019) 4282–4290, https://doi.org/10.1021/jacs.8b10795.
[21] E. Kim, L. Zwi-Dantsis, N. Reznikov, C.S. Hansel, S. Agarwal, M.M. Stevens, One-pot synthesis of multiple protein-encapsulated DNA flowers and their application in intracellular protein delivery, Adv. Mater. Deerfield Beach Fla 29 (2017), https://doi.org/10.1002/adma.201701086.
[22] Y. Jin, Z. Li, H. Liu, S. Chen, F. Wang, L. Wang, N. Li, K. Ge, X. Yang, X.-J. Liang, J. Zhang, Biodegradable, multifunctional DNAzyme nanoflowers for enhanced cancer therapy, NPG Asia Mater. 9 (2017), https://doi.org/10.1038/am.2017.34 e365–e365.
[23] C. Michiels, C. Tellier, O. Feron, Cycling hypoxia: a key feature of the tumor microenvironment, Biochim. Biophys. Acta 1866 (2016) 76–86, https://doi.org/10.1016/j.bbcan.2016.06.004.
[24] A. Hielscher, S. Gerecht, Hypoxia and free radicals: role in tumor progression and the use of engineering-based platforms to address these relationships, Free Radic. Biol. Med. 79 (2015) 281–291, https://doi.org/10.1016/j.freeradbiomed.2014.09.015.
[25] J. Zhang, Q. Zhang, Y. Lou, Q. Fu, Q. Chen, T. Wei, J. Yang, J. Tang, J. Wang, Y. Chen, X. Zhang, J. Zhang, X. Bai, T. Liang, Hypoxia-inducible factor-1α/interleukin-1β signaling enhances hepatoma epithelial-mesenchymal transition through macrophages in a hypoxic-inflammatory microenvironment, Hepatol. Baltim. Md 67 (2018) 1872–1889, https://doi.org/10.1002/hep.29681.
[26] X. Huang, J. Zhuang, S.W. Chung, B. Huang, G. Halpert, K. Negron, X. Sun, J. Yang, Y. Oh, P.M. Hwang, J. Hanes, J.S. Suk, Hypoxia-tropic protein nanocages for modulation of tumor- and chemotherapy-associated hypoxia, ACS Nano 13 (2019) 236–247, https://doi.org/10.1021/acsnano.8b05399.
[27] L. Liang, S. Xie, L. Jiang, H. Jin, S. Li, J. Liu, The Combined effects of hematoporphyrin monomethyl ether-SDT and doxorubicin on the proliferation of QBC939 cell lines, Ultrasound Med. Biol. 39 (1) (2013) 146–160, https://doi.org/10.1016/j.ultrasmedbio.2012.08.017.
[28] D. Song, W. Yue, Z. Li, J. Li, J. Zhao, N. Zhang, Study of the mechanism of sonodynamic therapy in a rat glioma model, OncoTargets Ther. 7 (2014) 1801–1810, https://doi.org/10.2147/OTT.S52426.
[29] X. Zheng, W. Liu, J. Ge, Q. Jia, F. Nan, Y. Ding, J. Wu, W. Zhang, C.-S. Lee, P. Wang, Biodegradable natural product-based nanoparticles for near-infrared fluorescence imaging-guided sonodynamic therapy, ACS Appl. Mater. Interfaces 11 (2019) 18178–18185, https://doi.org/10.1021/acsami.9b03270.
[30] G. Li, S. Wang, D. Deng, Z. Xiao, Z. Dong, Z. Wang, Q. Lei, S. Gao, G. Huang, E. Zhang, G. Zeng, Z. Wen, S. Wu, Z. Liu, Fluorinated chitosan to enhance transmucosal delivery of sonosensitizer-conjugated catalase for sonodynamic bladder cancer treatment post-intravesical instillation, ACS Nano 14 (2020) 1586–1599, https://doi.org/10.1021/acsnano.9b06689.
[31] P. Huang, X. Qian, Y. Chen, L. Yu, H. Lin, L. Wang, Y. Zhu, J. Shi, Metalloporphyrin-encapsulated biodegradable nanosystems for highly efficient

magnetic resonance imaging-guided sonodynamic cancer therapy, J. Am. Chem. Soc. 139 (2017) 1275–1284, https://doi.org/10.1021/jacs.6b11846.
[32] N.S. Al-Waili, G.J. Butler, J. Beale, R.W. Hamilton, B.Y. Lee, P. Lucas, Hyperbaric oxygen and malignancies: a potential role in radiotherapy, chemotherapy, tumor surgery and phototherapy, Med. Sci. Monit. Int. Med. J. Exp. Clin. Res. 11 (2005) 279–289.
[33] Q. Chen, L. Feng, J. Liu, W. Zhu, Z. Dong, Y. Wu, Z. Liu, Intelligent albumin-MnO2 nanoparticles as pH-/H2 O2 -responsive dissociable nanocarriers to modulate tumor hypoxia for effective combination therapy, Adv. Mater. Deerfield Beach Fla. 28 (2016) 7129–7136, https://doi.org/10.1002/adma.201601902.
[34] Y. Cheng, H. Cheng, C. Jiang, X. Qiu, K. Wang, W. Huan, A. Yuan, J. Wu, Y. Hu, Perfluorocarbon nanoparticles enhance reactive oxygen levels and tumour growth inhibition in photodynamic therapy, Nat. Commun. 6 (2015) 8785, https://doi.org/10.1038/ncomms9785.
[35] X. Song, L. Feng, C. Liang, K. Yang, Z. Liu, Ultrasound triggered tumor oxygenation with oxygen-shuttle nanoperfluorocarbon to overcome hypoxia-associated resistance in cancer therapies, Nano Lett. 16 (2016) 6145–6153, https://doi.org/10.1021/acs.nanolett.6b02365.
[36] T. Gu, L. Cheng, F. Gong, J. Xu, X. Li, G. Han, Z. Liu, Upconversion composite nanoparticles for tumor hypoxia modulation and enhanced near-infrared-triggered photodynamic therapy, ACS Appl. Mater. Interfaces 10 (2018) 15494–15503, https://doi.org/10.1021/acsami.8b03238.
[37] O.D. Saugstad, Hyperoxia in the term newborn: more evidence is still needed for optimal oxygen therapy, Acta Paediatr. Oslo Nor 101 (2012) (1992) 34–38, https://doi.org/10.1111/j.1651-2227.2011.02546.x.
[38] G. Vindigni, S. Raniolo, F. Iacovelli, V. Unida, C. Stolfi, A. Desideri, S. Biocca, AS1411 aptamer linked to DNA nanostructures diverts its traffic inside cancer cells and improves its therapeutic efficacy, Pharmaceutics 13 (2021) 1671, https://doi.org/10.3390/pharmaceutics13101671.
[39] H. Zhao, J. Lv, F. Li, Z. Zhang, C. Zhang, Z. Gu, D. Yang, Enzymatical biomineralization of DNA nanoflowers mediated by manganese ions for tumor site activated magnetic resonance imaging, Biomaterials 268 (2021) 120591, https://doi.org/10.1016/j.biomaterials.2020.120591.
[40] M. Maeda, Y. Muragaki, J. Okamoto, S. Yoshizawa, N. Abe, H. Nakamoto, H. Ishii, K. Kawabata, S. Umemura, N. Nishiyama, K. Kataoka, H. Iseki, Sonodynamic therapy based on combined use of low dose administration of epirubicin-incorporating drug delivery system and focused ultrasound, Ultrasound Med. Biol. 43 (2017) 2295–2301, https://doi.org/10.1016/j.ultrasmedbio.2017.06.003.
[41] K. Zhang, H. Xu, X. Jia, Y. Chen, M. Jia, L. Sun, H. Chen, Ultrasound-triggered nitric oxide release platform based on energy transformation for targeted inhibition of pancreatic tumor, ACS Nano 10 (12) (2016) 10816–10828, https://doi.org/10.1021/acsnano.6b04921.
[42] R. Pirker, Chemotherapy remains a cornerstone in the treatment of nonsmall cell lung cancer, Curr. Opin. Oncol. 32 (2020) 63–67, https://doi.org/10.1097/CCO.0000000000000592.
[43] M. Norouzi, V. Yathindranath, J.A. Thliveris, D.W. Miller, Salinomycin-loaded iron oxide nanoparticles for glioblastoma therapy, Nanomater. Basel Switz. 10 (2020) 477, https://doi.org/10.3390/nano10030477.
[44] S. Ghosh, A. Javia, S. Shetty, D. Bardoliwala, K. Maiti, S. Banerjee, A. Khopade, A. Misra, K. Sawant, S. Bhowmick, Triple negative breast cancer and non-small cell lung cancer: clinical challenges and nano-formulation approaches, J. Contr. Release 337 (2021) 27–58, https://doi.org/10.1016/j.jconrel.2021.07.014.
[45] L. Harrison, K. Blackwell, Hypoxia and anemia: factors in decreased sensitivity to radiation therapy and chemotherapy? Oncol. 9 (Suppl 5) (2004) 31–40, https://doi.org/10.1634/theoncologist.9-90005-31.
[46] T. Thambi, J.H. Park, D.S. Lee, Hypoxia-responsive nanocarriers for cancer imaging and therapy: recent approaches and future perspectives, Chem. Commun. Camb. Engl. 52 (2016) 8492–8500, https://doi.org/10.1039/c6cc02972h.
[47] J. Zhou, T. Schmid, S. Schnitzer, B. Brüne, Tumor hypoxia and cancer progression, Cancer Lett. 237 (2006) 10–21, https://doi.org/10.1016/j.canlet.2005.05.028.
[48] Y. Lv, R. Hu, G. Zhu, X. Zhang, L. Mei, Q. Liu, L. Qiu, C. Wu, W. Tan, Preparation and biomedical applications of programmable and multifunctional DNA nanoflowers, Nat. Protoc. 10 (2015) 1508–1524, https://doi.org/10.1038/nprot.2015.078.
[49] S. Han, J.S. Lee, J.B. Lee, Synthesis of a multi-functional DNA nanosphere barcode system for direct cell detection, Nanoscale 9 (2017) 14094–14102, https://doi.org/10.1039/c7nr03615a.
[50] N. Kim, E. Kim, H. Kim, M.R. Thomas, A. Najer, M.M. Stevens, Tumor-targeting cholesterol-decorated DNA nanoflowers for intracellular ratiometric aptasensing, Adv. Mater. Deerfield Beach Fla. 33 (2021) e2007738, https://doi.org/10.1002/adma.202007738.
[[5][1] C. Pérez-Arnaiz, N. Busto, J.M. Leal, B. García, New insights into the mechanism of the DNA/doxorubicin interaction, J. Phys. Chem. B 118 (2014) 1288–1295, https://doi.org/10.1021/jp411429g.
[52] M. Alibolandi, M. Ramezani, K. Abnous, F. Hadizadeh, AS1411 aptamer-decorated biodegradable polyethylene glycol-poly(lactic-co-glycolic acid) nanopolymersomes for the targeted delivery of gemcitabine to non-small cell lung cancer in vitro, J. Pharm. Sci. 105 (2016) 1741–1750, https://doi.org/10.1016/j.xphs.2016.02.021.
[53] E.J. Joo, G.B. ten Dam, T.H. van Kuppevelt, T. Toida, R.J. Linhardt, Y.S. Kim, Nucleolin: acharan sulfate-binding protein on the surface of cancer cells, Glycobiology 15 (2005) 1–9, https://doi.org/10.1093/glycob/cwh132.
[54] L. Fruk, C.M. Niemeyer, Covalent hemin-DNA adducts for generating a novel class of artificial heme enzymes, Angew. Chem. Int. Ed Engl. 44 (2005) 2603–2606, https://doi.org/10.1002/anie.200462567.
[55] M. Glettenberg, C.M. Niemeyer, Tuning of peroxidase activity by covalently tethered DNA oligonucleotides, Bioconjug. Chem. 20 (2009) 969–975, https://doi.org/10.1021/bc800558g.
[56] A. Janoniene, Z. Liu, L. Baranauskiene, E. Mäkilä, M. Ma, J. Salonen, J. Hirvonen, H. Zhang, V. Petrikaite, H.A. Santos, A versatile carbonic anhydrase IX targeting ligand-functionalized porous silicon nanoplatform for dual hypoxia cancer therapy and imaging, ACS Appl. Mater. Interfaces 9 (2017) 13976–13987, https://doi.org/10.1021/acsami.7b04038.
[57] G.L. Semenza, HIF-1 mediates metabolic responses to intratumoral hypoxia and oncogenic mutations, J. Clin. Invest. 123 (2013) 3664–3671, https://doi.org/10.1172/JCI67230.
[58] M. Hahne, P. Schumann, M. Mursell, C. Strehl, P. Hoff, F. Buttgereit, T. Gaber, Unraveling the role of hypoxia-inducible factor (HIF)-1α and HIF-2α in the adaption process of human microvascular endothelial cells (HMEC-1) to hypoxia: redundant HIF-dependent regulation of macrophage migration inhibitory factor, Microvasc. Res. 116 (2018) 34–44, https://doi.org/10.1016/j.mvr.2017.09.004.
[59] P. Lertkiatmongkol, D. Liao, H. Mei, Y. Hu, P.J. Newman, Endothelial functions of platelet/endothelial cell adhesion molecule-1 (CD31), Curr. Opin. Hematol. 23 (2016) 253–259, https://doi.org/10.1097/MOH.0000000000000023.

Abbreviations

DOX/HRP-DFs: DNA nanoflowers encoding AS1411 aptamer and encapsulating chemotherapeutic drug doxorubicin and oxygen-producing drug horseradish peroxidase
DOX: Doxorubicin
SDT: Sonodynamic Therapy
ROS: Reactive Oxygen Species
O2: Oxygen
HRP: Horseradish Peroxidase
FBS: Fetal Bovine Serum
CCK-8: Cell Counting Kit-8
LLC: Lewis Lung Carcinoma
HRP-DFs: HRP-encapsulated DNA Nanoflowers
BSA: Bovine Serum Albumin
SEM: Scanning Electron Microscopy
TEM: Transmission Electron Microscopy
DLS: Dynamic Light Scattering
EDS: Energy-dispersive X-ray Spectroscopy
CLSM: Confocal Laser Scanning Microscopy
DAPI: 4′,6-diamidino-2-phenylindole
H&E: Hematoxylin-eosin
TUNEL: TdT-mediated dUTP nick-end labeling
HIF-1α: Hypoxia-inducible Factor-1alpha
VEGF: Vascular Endothelial Growth Factor
PECAM-1/CD31: Platelet Endothelial Cell Adhesion Molecule-1
ALT: Alanine Aminotransferase
AST: Aspartate Aminotransferase
BUN: Blood Urea Nitrogen
CREA: Creatinine
CK: Creatine Kinase
TBIL: Total Bilirubin
SD: Standard Deviation